

Simulating stochastic population dynamics: The Linear Noise Approximation can capture non-linear phenomena

Frederick Truman-Williams^a and Giorgos Minas^{b,1}

^a*Mathematical Institute, University of Oxford, Oxford, OX2 6GG, United Kingdom*

^b*School of Mathematics and Statistics, University of St Andrews, St Andrews, KY16 9SS, Scotland, United Kingdom**

Abstract

Population dynamics in fields such as molecular biology, epidemiology, and ecology exhibit highly stochastic and non-linear behavior. In gene regulatory systems in particular, oscillations and multistability are especially common. Despite this, none of the currently available stochastic models for population dynamics are both accurate and computationally efficient for long-term predictions. A prominent model in this field, the Linear Noise Approximation (LNA), is computationally efficient for tasks such as simulation, sensitivity analysis, and parameter estimation; however, it is only accurate for linear systems and short-time predictions. Other models may achieve greater accuracy across a broader range of systems, but they sacrifice computational efficiency and analytical tractability. This paper demonstrates that, with specific modifications, the LNA can accurately capture non-linear dynamics in population processes. We introduce a new framework based on centre manifold theory, a classical concept from non-linear dynamical systems. This approach enables the identification of simple, system-specific modifications to the LNA, tailored to classes of qualitatively similar non-linear dynamical systems. With these modifications, the LNA can achieve accurate long-term simulations without compromising computational efficiency. We apply our methodology to classes of oscillatory and bi-stable systems, and present multiple examples from molecular population dynamics that demonstrate accurate long-term simulations alongside significant improvements in computational efficiency.

1 Introduction

In molecular biology, ecology, epidemiology and other fields, there is a multitude of non-linear dynamical phenomena such as oscillations and multi-stabilities. Examples include circadian rhythms [23], embryonic development oscillations [43], cell signalling oscillations [4], multi-stabilities in the cell cycle [50, 52, 2], cell differentiation [9, 21], and apoptosis [3], the central carbon metabolism in *E.coli* [28], predator-prey oscillations in ecology [13], and epidemic oscillations [70]. These non-linear dynamics are caused by feed-forward loops [42], negative feedback loops [42, 54] and other mechanisms, which are operated by networks of interacting species. For example, gene expression oscillations are often generated when a gene directly suppresses its own expression or activates the expression of its suppressors. In infectious diseases outbreaks, compartments of the population, such as infected and susceptible individuals, interact between each other and phenomena like awareness and fatigue can generate oscillatory behaviors [70].

*To whom correspondence should be addressed. E-mail: gm256@st-andrews.ac.uk

The effects of stochasticity in interactions between different populations—arising from molecular diffusion or, more generally, from the complex environments in which these interactions occur—are significant, particularly for small populations. Yet modeling this stochasticity using fast, accurate, and scalable methods remains an unsolved problem.

The networks of stochastic interactions between different populations are often called reaction networks. The term reaction is not only used for biochemical reactions but any event that directly causes a change in the population of one or more species or groups. The stochastic dynamics of reaction networks, can be described, under certain assumptions, by a Markov process $\{\mathbf{Y}(t) = (Y_1(t), \dots, Y_n(t))^T : t \geq 0\}$, describing the evolution of n different populations over time. The so-called (chemical) master equation [15], which describes the evolution of the probability distribution of the species populations over time, is analytically solvable only in rare cases, severely limiting its tractability. The stochastic simulation algorithm (SSA), also known as the Gillespie algorithm [16], produces exact simulations of the Markov process $\{\mathbf{Y}(t) : t \geq 0\}$ but it is far too slow to be used in most applied settings since it simulates every single reaction event.

At present, there are several methods available for approximating the master equation, which aim to accelerate simulations. Notable examples include tau leaping algorithms [19, 20] and the numerical integration of the chemical Langevin equations [18]. Both of these approaches significantly increase simulation speed; however, they leave no scope for the analytical study of the probability distributions of the populations and can be extremely slow for sensitivity analysis and parameter estimation. Other recent methods [7, 30] focus on simplifying protein-binding reactions, which frequently appear in molecular biology networks.

Much work has followed from van Kampen’s system size expansion [66], which uses a system size parameter Ω (like cell volume in molecular biology, maximum population size in ecology or epidemiology) to derive approximations of the master equation. Under certain conditions, the deterministic process $\{\mathbf{x}(t) = (x_1(t), \dots, x_n(t))^T : t \geq 0\}$ which solves the macroscopic reaction-rate equations was shown to be the law of large numbers limit, as $\Omega \rightarrow \infty$, of the Markov process governed by the master equation [34, 35]. The Linear Noise Approximation (LNA), derived using the system size expansion method, is a stochastic model that provides even more rapid simulation than the aforementioned stochastic methods as well as being the only model in this field that allows analytical expressions of probability distributions of populations at arbitrary time-points. This makes the LNA a powerful tool for sensitivity analysis and statistical inference [46, 47, 61, 48, 33, 12, 22, 55]. However, the important drawback of using the LNA is its inability to approximate the long-term behavior of non-linear population dynamics. Indeed, when the system dynamics are non-linear [69], predictions of the state of the system at time t given the state at an earlier time s , $0 < s < t$, become inaccurate as $t - s$ becomes large.

For any given system, we can qualitatively examine the dynamics of its paths and identify different phases in the populations’ evolution—for instance their peaks and troughs. If we were to examine the distribution of entire stochastic paths generated by the SSA in a finite number of time-points then we find that, the phases of such paths become out of sync with what the LNA predicts their phases to be. Hence the LNA makes incorrect predictions of the dynamics thereafter. In [46], it was shown that in the specific setting where the macroscopic ($\Omega \rightarrow \infty$) deterministic approximation has an attractive limit cycle solution, correcting these drifts in phase predicted by the LNA is sufficient to produce simulations that are nearly identical to those produced by the SSA. This approach enables the construction of both fast and accurate algorithms for stochastic simulation, sensitivity analysis, and statistical inference of this class of non-linear systems [46].

The main results of this paper are the following. Firstly, we develop a novel framework for constructing LNA-based models for non-linear dynamical systems. We adopt the term phase corrected LNA (pcLNA)—originally introduced in [46]—to describe this stochastic modelling

approach, which evolves the system using LNA equations while periodically adjusting the phase to mitigate phase drift. Fundamental to the pcLNA approach is a mapping G that computes the phase of any stochastic state allowing for any phase drift to be corrected. We show that, for any parameter-dependent system whose macroscopic reaction-rate equation admits a non-hyperbolic equilibrium for some parameter value, tools from dynamical systems theory can be used to explicitly construct the phase-correcting map G . Notably, by combining results from [51, 62] with Itô’s Lemma [38], we derive a novel decomposition of the LNA stochastic process into coordinates exhibiting non-linear, persistent dynamics and coordinates with transient dynamics. This decomposition suggests that a common phase definition can be used for classes of stochastic systems with qualitatively similar behavior. Using these findings, we provide a step-by-step procedure for defining a phase-correcting map and a general algorithm to be used for stochastic simulation.

Secondly, we use this framework to provide readily applicable algorithms that can accurately simulate long-term stochastic dynamics for arguably the two most abundant non-linear phenomena: oscillations and bi-stability. We demonstrate this on several systems including the oscillatory systems in [39, 71, 4], and bi-stable systems in [14, 2, 21]. Here the pcLNA model offers accurate approximations of the master equation for long-term simulation whilst substantially reducing the simulation time by several orders of magnitude. We also propose a fast method to predict the speed of SSA simulations, and therefore assess whether a faster simulation method is necessary.

We emphasize that with further development on defining explicit phase-correcting maps G , the pcLNA framework introduced here could be used to simulate other class of non-linear dynamical systems with computational efficiency and accuracy. We also note that a key implication of the speed and accuracy of pcLNA is that it enables the approach to be used for computationally intensive tasks such as sensitivity analysis, inference, and prediction for large, non-linear systems.

While the approach developed in [46] demonstrated that phase correction significantly improves the long-term accuracy of the LNA in oscillatory systems with stable limit cycles, it was limited to this specific dynamics. In contrast, the framework introduced in this paper generalises the concept of phase correction by introducing centre manifold theory to define and correct phase drifts to a broad class of systems only assumed to have a non-hyperbolic equilibrium, which includes the abundant classes of oscillatory and bi-stable systems.

We begin in Section 2 with a review of stochastic population dynamics evolving through reaction networks (Section 2.1) and the system size expansion (Section 2.2), and then introduce the Linear Noise Approximation (LNA) in Section 2.3. We conclude the section by discussing the LNA’s loss of accuracy in non-linear systems. In Section 3, we introduce the phase corrected Linear Noise Approximation framework. To understand the LNA’s failure we define the notion of phase in the context of stochastic reaction networks (Section 3.1) before presenting the general phase corrected LNA (pcLNA) simulation algorithm in Section 3.2. We follow this by a discussion on how to define the phase-correcting map in Section 3.3. In Section 4, we apply our framework to reaction networks whose macroscopic reaction rate equation undergoes a Hopf bifurcation and develop the pcLNA algorithm specific to these systems. Section 5 focuses on bi-stable systems and constructs the corresponding pcLNA algorithm. We validate our framework through numerical investigations in Section 6, and conclude with a discussion of our findings and future directions in Section 7. Additional numerical investigations demonstrating the accuracy of the pcLNA modelling techniques on other reaction networks, as well as supporting technical results and derivations, are provided in the Supporting Information (SI).

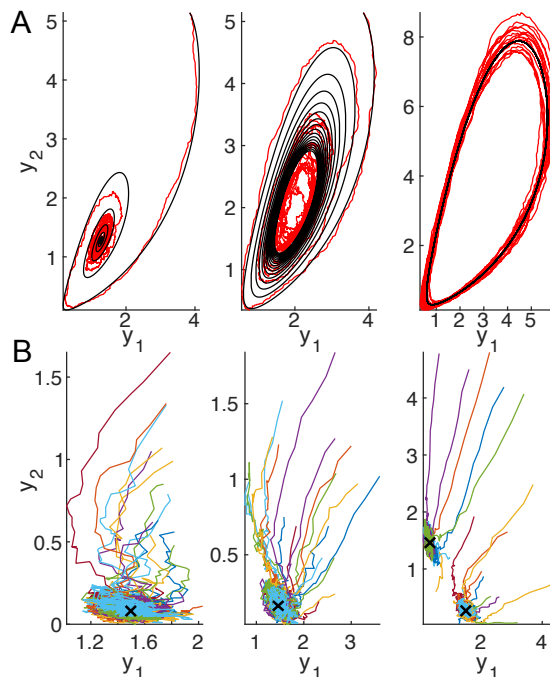


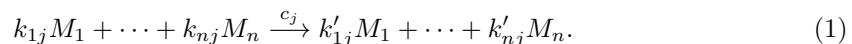
Figure 1: A. Phase portraits of solutions of the RRE in (6) (black) and a SSA simulation (red) for the system in [71]. B. Phase portraits of 20 SSA simulations (color) and the equilibria of the RRE in (6) (crosses) for the system in [14]. The qualitative changes from left to right figure are due to changes in the bifurcation parameter value.

2 Population dynamics

We begin by reviewing, in Sections 2.1-2.3, the mathematical formulation of population dynamics evolving through reaction networks. Our discussion is restricted to the concepts needed for the development of our methodology; for a more comprehensive review, see [1, 45, 72]. We describe this formulation within the context of molecular biology, although analogous terminology can be applied in other fields such as epidemiology and ecology (see, for instance, [22, 72] and Figure 2).

2.1 Reaction networks

A system of n different molecular species, M_1, M_2, \dots, M_n has state vector, $\mathbf{Y}(t) = (Y_1(t), \dots, Y_n(t))^{\top}$ where $Y_i(t)$, $i \in \{1, \dots, n\}$, denotes the number of molecules (i.e. the population) of species M_i at time t and \top denotes the transpose. These molecules undergo reactions R_j , $j \in \{1, \dots, r\}$, such as transcription, translation, degradation and translocation, which change the number of molecules of each species,



Here, the non-negative integer coefficients k_{ij} and k'_{ij} denote the number of molecules of species M_i involved as reactants and products, respectively, in reaction R_j . If R_j occurs at time $t \geq 0$, $\mathbf{Y}(t)$ jumps to a new state $\mathbf{Y}(t) + \boldsymbol{\nu}_j$, where the integer transition vectors $\boldsymbol{\nu}_j = (k'_{1j} - k_{1j}, \dots, k'_{nj} - k_{nj})^{\top}$ are often called stoichiometric. Under the assumption that these reactions occur in a

well-mixed solution [16], we can derive the propensity functions $\pi_j : \mathbb{R}^n \rightarrow [0, \infty)$ for each $j \in \{1, \dots, r\}$ with the probability of one R_j reaction occurring in the next infinitesimal time interval $[t, t + dt)$

$$P(\mathbf{Y}(t + dt) - \mathbf{Y}(t) = \boldsymbol{\nu}_j) = \pi_j(\mathbf{Y}(t))dt + o(dt^2). \quad (2)$$

The propensity functions π_j along with the stoichiometric vector $\boldsymbol{\nu}_j$, $j = 1, \dots, r$, completely specify the evolution of the reaction network.

The general form of the propensity function of the reaction in (1), when $\mathbf{Y}(t) = \mathbf{y} = (y_1, \dots, y_n)$ is $\pi_j(\mathbf{y}) = c_j \prod_i \binom{y_i}{k_{ij}}^1$. Uni-molecular ($M_i \xrightarrow{c_j} \cdot$) and bi-molecular ($M_i + M_{i'} \xrightarrow{c_j} \cdot$) reactions, with propensities $c_j y_i$ and $c_j y_i y_{i'}$ respectively, are the most common type (see [68]). Here $c_j > 0$ is the reaction rate constant corresponding to reaction R_j . The propensity functions are not restricted to the above general form. For instance, for enzymatic reactions involving species M_i the propensity has the Michaelis-Menten form [31], $c_2 y_i / (c_1 + y_i)$, while the Hill form [26], $c_2 y_i^h / (c_1^h + y_i^h)$, is also often used to reflect cooperative binding. For a discussion on the latter forms of propensities see [7].

These conditions give rise to a time-inhomogeneous, discrete state-space Markov process $\{\mathbf{Y}(t) : t \geq 0\}$. The Kolmogorov forward equation [17] describing the evolution of the probability distribution, $P(\mathbf{y}, t) := P(\mathbf{Y}(t) = \mathbf{y} \mid \mathbf{Y}(0) = \mathbf{y}_0)$, of the stochastic process $\{\mathbf{Y}(t) : t \geq 0\}$,

$$\frac{\partial P(\mathbf{y}, t)}{\partial t} = \sum_{j=1}^r \pi_j(\mathbf{y} - \boldsymbol{\nu}_j) P(\mathbf{y} - \boldsymbol{\nu}_j, t) - \sum_{j=1}^r \pi_j(\mathbf{y}) P(\mathbf{y}, t), \quad (3)$$

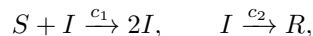
is often referred to as the (chemical) master equation. Despite the equation only being analytically tractable for few cases, exact trajectories can be generated using Gillespie's stochastic simulation algorithm (SSA) [16]. We provide details of this in SI (Section S1).

Equivalently, the process can be represented via the random time change representation (RTC) [1]

$$\mathbf{Y}(t) = \mathbf{Y}(0) + \sum_{j=1}^r \boldsymbol{\nu}_j N_j \left(\int_0^t \pi_j(\mathbf{Y}(s)) ds \right), \quad (4)$$

where N_j , $j \in \{1, \dots, r\}$, are independent, unit-rate Poisson processes corresponding to reaction R_j . For a given trajectory $\mathbf{y}(s)$, $s \in [0, t)$, the random variables $N_j \left(\int_0^t \pi_j(\mathbf{y}(s)) ds \right)$ are independent and have Poisson distribution with mean $\int_0^t \pi_j(\mathbf{y}(s)) ds$.

Example (SIR model) The SIR model used to describe population dynamics in infectious disease outbreaks is an example of a reaction network. We formulate it here to provide a concrete instance of the general framework introduced above (see also Figure 2(A-B) for a summary). In the SIR network, there are three populations, say M_1, M_2, M_3 , corresponding to the Susceptible (S), Infected (I), and Recovered (R) individuals. Two reactions can occur—infection (R_c) and recovery (R_2)—which can be represented as



where c_1 and c_2 are the reaction rate constants for the two reactions. The state vector $\mathbf{Y} = (Y_1, Y_2, Y_3)^\top$ represents the three populations M_1 (S), M_2 (I), and M_3 (R). The propensity functions are

$$\pi_1(\mathbf{Y}) = c_1 Y_1 Y_2, \quad \pi_2(\mathbf{Y}) = c_2 Y_2$$

with corresponding stoichiometry vectors $\mathbf{v}_1 = (-1, +1, 0)^\top$ and $\mathbf{v}_2 = (0, -1, +1)^\top$. This can be used to formulate Equations (3) and (4) for this system.

¹ $\binom{n}{k}$ is the binomial coefficient of n choose k .

2.2 System Size Expansion

Following the work of [34] and [66], it is common in seeking methods to approximate the process $\{\mathbf{Y}(t) : t \geq 0\}$, to introduce a system size parameter Ω . Through setting $\mathbf{X}(t) := \mathbf{Y}(t)/\Omega$, one can study the dependence of stochastic fluctuations upon system size. It is sufficient to assume that the rates $\pi_j(\mathbf{Y}(t))$ depend upon Ω as $\pi_j(\mathbf{Y}(t)) := \Omega \rho_j(\mathbf{Y}(t)/\Omega)$ where $\rho_j : \mathbb{R}^n \rightarrow [0, \infty)$ are called macroscopic rates of the system and are smooth. This is a fairly-relaxed condition, that can be further relaxed to more general relations between the two functions [66, 35].

Using this condition, we can re-write the infinitesimal RTC equation in (4) in terms of $\mathbf{X}(t)$ as

$$\mathbf{X}(t + dt) - \mathbf{X}(t) = \sum_{j=1}^r \frac{\nu_j}{\Omega} N_j(\Omega \rho_j(\mathbf{X}(t)) dt), \quad dt > 0 \quad (5)$$

with $\mathbf{X}(0) = \mathbf{X}_0$, thus providing a time evolution law for the process $\{\mathbf{X}(t) : t \geq 0\}$. If, for each $t \geq 0$, we define $\mathbf{x}(t)$ as the limit in probability of $\mathbf{X}(t)$ as $\Omega \rightarrow \infty$, we can use the law of large numbers² (see [34, 35]) to derive the limit of equation (5), as $\Omega \rightarrow \infty$,

$$\mathbf{x}(t + dt) - \mathbf{x}(t) = \sum_{j=1}^r \nu_j \rho_j(\mathbf{x}(t)) dt, \quad \mathbf{x}(0) = \mathbf{x}_0.$$

Letting $dt \rightarrow 0$ we derive the macroscopic reaction rate equation (RRE), corresponding to the classical mass-action kinetics. Typical in applied biochemical settings is the need to study the qualitative changes in the dynamics of $\{\mathbf{X}(t) : t \geq 0\}$ and $\{\mathbf{x}(t) : t \geq 0\}$ when one (or more) of the system parameters – typically reaction rate constants – are allowed to vary smoothly. Let this parameter be given by $\alpha \in \mathbb{R}$ and write the RRE as

$$\dot{\mathbf{x}} = \frac{d\mathbf{x}}{dt} = \mathbf{F}(\mathbf{x}, \alpha), \quad \mathbf{F}(\mathbf{x}, \alpha) := \sum_{j=1}^r \nu_j \rho_j(\mathbf{x}(t), \alpha), \quad \mathbf{x}(0) = \mathbf{x}_0. \quad (6)$$

where both ρ_j and F depend smoothly on \mathbf{x} and α . The corresponding Jacobian matrix is

$$\mathbf{J} = \mathbf{J}(\mathbf{x}, \alpha) = (\partial F_i / \partial x_j)_{i,j=1}^n. \quad (7)$$

We will refer to the parameter α as the bifurcation parameter.

Example (SIR model, continued) If we define a system size parameter Ω (e.g. total population) for the SIR model above, then we can apply system size expansion. The reaction rates are set to satisfy $\pi_j(\mathbf{Y}(t)) := \Omega \rho_j(\mathbf{Y}(t)/\Omega)$, and hence for $\mathbf{x} = \mathbf{Y}/\Omega$ we get

$$\begin{aligned} \pi_1(\mathbf{Y}) &= c_1 Y_1 Y_2 = \Omega \tilde{c}_1 x_1 x_2 = \Omega \rho_1(\mathbf{x}), & \rho_1(\mathbf{x}) &= \tilde{c}_1 x_1 x_2, & \tilde{c}_1 &= \Omega c_1 \\ \pi_2(\mathbf{Y}) &= c_2 Y_2 = \Omega c_2 x_2 = \Omega \rho_2(\mathbf{x}), & \rho_2(\mathbf{x}) &= c_2 x_2 \end{aligned}$$

which together with the stoichiometry vectors give the RRE

$$\begin{aligned} \dot{x}_1 &= dx_1/dt = -\tilde{c}_1 x_1 x_2 \\ \dot{x}_2 &= dx_2/dt = +\tilde{c}_1 x_1 x_2 - c_2 x_2 \\ \dot{x}_3 &= dx_3/dt = +c_2 x_2. \end{aligned}$$

²Note that for a sequence X_1, X_2, \dots , of independent Poisson random variables with mean $0 < \lambda < \infty$, $N^{-1} \sum_{i=1}^N X_i$ converges in probability to λ , as $N \rightarrow \infty$.

2.3 The Linear Noise Approximation (LNA)

To take into account the stochasticity of interactions between (molecular or other) populations, one approach is to define the LNA ansatz equation [66, 34, 35] that describes the relation between the stochastic process $\{\mathbf{X}(t) : t \geq 0\}$ and a deterministic solution $\gamma = \{\mathbf{x}(t) : t \geq 0\}$ of the RRE system in (6). Their difference, scaled by $\Omega^{-1/2}$, is a stochastic process, $\{\boldsymbol{\xi}(t) : t \geq 0\}$, with $\boldsymbol{\xi}(t)$ quantifying the noisy deviations away from $\mathbf{x}(t)$. That is, for each $t \geq 0$,

$$\mathbf{X}(t) = \mathbf{x}(t) + \Omega^{-1/2}\boldsymbol{\xi}(t). \quad (8)$$

The time-evolution of $\{\boldsymbol{\xi}(t), t \geq 0\}$, for sufficiently large Ω , can be described (see [49] or SI, section S2 for the derivation details) by the linear Stochastic Differential equation (SDE) in the Itô sense

$$d\boldsymbol{\xi} = \mathbf{J}_t\boldsymbol{\xi}dt + \mathbf{E}_t d\mathbf{B}_t, \quad (9)$$

where $\mathbf{J}_t = \mathbf{J}(\mathbf{x}(t))$ is the Jacobian matrix in (7) evaluated at $\mathbf{x}(t)$, \mathbf{B}_t an r -dimensional Wiener process [72], and

$$\mathbf{E}_t = \mathbf{E}(\mathbf{x}(t)) = \mathbf{S}\text{diag}\left(\sqrt{\rho_1(\mathbf{x}(t))}, \dots, \sqrt{\rho_r(\mathbf{x}(t))}\right) \quad (10)$$

the product of the stoichiometry matrix $\mathbf{S} = [\boldsymbol{\nu}_1 \cdots \boldsymbol{\nu}_r]$, and the square root of the diagonal matrix, with main diagonal entries the reaction rates $(\rho_1(\mathbf{x}(t)), \dots, \rho_r(\mathbf{x}(t)))$. This linear SDE in (9) has a solution that, for $0 \leq s \leq t < \infty$, can be written as

$$\boldsymbol{\xi}(t) = \mathbf{C}(s, t)\boldsymbol{\xi}(s) + \boldsymbol{\eta}(s, t), \quad \boldsymbol{\eta}(s, t) \sim \text{MVN}(\mathbf{0}, \mathbf{D}(s, t)), \quad (11)$$

where $\mathbf{C}(s, t)$ the fundamental matrix of (6), i.e. the solution of the initial value problem

$$\dot{\mathbf{C}} = \mathbf{J}_t\mathbf{C}, \quad \mathbf{C}(s, s) = \mathbf{I}, \quad (12)$$

and $\mathbf{D}(s, t)$ the symmetric, positive-definite matrix that is a solution of the initial value problem

$$\dot{\mathbf{D}} = \mathbf{J}_t\mathbf{D} + \mathbf{D}\mathbf{J}_t^\top + \mathbf{E}_t\mathbf{E}_t^\top, \quad \mathbf{D}(s, s) = \mathbf{0}. \quad (13)$$

Here we write \mathbf{I} for the identity matrix and $\mathbf{0}$ for the zero matrix. We also write $\text{MVN}(\mathbf{m}, \mathbf{S})$ for the Multivariate Normal (Gaussian) distribution with mean \mathbf{m} , and variance matrix \mathbf{S} .

The above representation implies that by solving the initial value problems in (6), (12) and (13), and starting with an initial condition for $\boldsymbol{\xi}(0) = \boldsymbol{\xi}_0$ drawn from an arbitrary MVN distribution, one can easily derive the MVN probability distribution of $\boldsymbol{\xi}(t)$, for any time $t > 0$. In this case, we say that the LNA prediction for $\mathbf{X}(t)$ was initialised at time $s = 0$. The process $\{\mathbf{X}(t) : t \geq 0\}$ modeled by the LNA is only an approximation of the true dynamics of the reaction network $\{\mathbf{Y}(t)/\Omega : t \geq 0\}$ where $\{\mathbf{Y}(t) : t \geq 0\}$ evolves according to (4).

Therefore, when we refer to the notion of accuracy, we mean the accuracy in the distribution of $\mathbf{X}(t)$ when trying to capture the distribution of $\mathbf{Y}(t)/\Omega$ for each $t \geq 0$, where $\{\mathbf{Y}(t) : t \geq 0\}$ evolves according to (4).

Example (SIR model, continued): To apply the LNA to the SIR reaction network, we first need to compute the Jacobian matrix by differentiation, which gives

$$\mathbf{J} = \begin{pmatrix} -\tilde{c}_1x_2 & -\tilde{c}_1x_1 & 0 \\ \tilde{c}_1x_2 & \tilde{c}_1x_1 - c_2 & 0 \\ 0 & c_2 & 0 \end{pmatrix}$$

and the matrix defined in (10), which is

$$\mathbf{E} = \begin{pmatrix} -1 & 0 \\ +1 & -1 \\ 0 & +1 \end{pmatrix} \begin{pmatrix} \sqrt{\tilde{c}_1 x_1 x_2} & 0 \\ 0 & \sqrt{c_2 x_2} \end{pmatrix} = \begin{pmatrix} -\sqrt{\tilde{c}_1 x_1 x_2} & 0 \\ \sqrt{\tilde{c}_1 x_1 x_2} & -\sqrt{c_2 x_2} \\ 0 & \sqrt{c_2 x_2} \end{pmatrix}.$$

These matrices depend on the solution, $\{\mathbf{x}(t) = (x_1(t), x_2(t), x_3(t))^\top : t \geq 0\}$, of the RRE in (6). Solving (12) and (13) using the above matrices gives the matrices $\mathbf{C}(s, t)$ and $\mathbf{V}(s, t)$ required to derive the distribution of $\boldsymbol{\xi}(t)$ in (11) and in turn the state $\mathbf{X}(t)$ in (8).

2.3.1 Accuracy of the LNA

The LNA accurately approximates the master equation in specific contexts. As discussed in SI (see section S2), the LNA is derived using the Central Limit Theorem, as Ω tends to ∞ , as an approximation of the probability distribution function satisfying the master equation. As a result, we expect the LNA to be accurate when Ω is sufficiently large. The value of Ω needed to ensure accuracy depends on the characteristics of the system's dynamics and the length of time interval where the approximation is sought.

For any given finite Ω , if the LNA accurately represents the distribution of the state of a given system at some time-point, it is expected to maintain this accuracy for a subsequent short time interval (see [69]). The duration for which the LNA remains accurate is influenced by the dynamics of the system and the level of stochasticity present. For instance, it was observed in [46] that for periodic systems with a moderate size Ω , the time interval over which the LNA retains its accuracy is approximately equal to the period of the system.

In situations where the system displays linear dynamics (i.e. the propensity functions in (2) are linear with respect to $\mathbf{Y}(t)$) the first two moments of the LNA coincide with those of solutions of the master equation [40]. Additionally, empirical studies comparing the distribution of the system at specific time-points, as predicted by the LNA, with histograms of the state distribution derived by simulated trajectories using the SSA, have shown agreement when the initial conditions are in the vicinity of stable equilibrium points (see for instance, [64, 46, 57], and Figure 2(B)). Recent results identified the precise generic conditions under which the LNA is accurate near equilibrium points [24].

It is important to note that, for moderate system sizes, the LNA tends to fail in approximating the long-term dynamics of multi-stable and oscillatory systems (see [57, 5, 29, 64, 46] and Figure 2(C-D)). We further discuss the failure of the LNA in Section 3.1.

3 The phase corrected Linear Noise Approximation (pcLNA)

In this section, we develop the phase corrected Linear Noise Approximation (pcLNA) algorithm for stochastic simulation of population dynamics. We begin by introducing a general definition of phase.

3.1 Phase

Important in diagnosing this failure of the LNA approximation, and indeed the rest of this paper, is the idea of phase. Existing definitions of phase for stochastic systems typically extend the concept of phase for noisy limit cycles [56, 6, 11]. Here we introduce a definition suitable for any non-linear dynamics arising from the RRE (6), including systems with oscillations or multistability.

We use the term *phase* in its common-language sense: a stage in a dynamic process. To define the phase of an arbitrary point \mathbf{X} on a stochastic trajectory $\{\mathbf{X}(t) : t \geq 0\}$, we compare it with a set of reference trajectories

$$\Gamma = \bigcup_{\ell=1}^L \{\mathbf{x}^{(\ell)}(t) : t \geq 0\}, \quad L \geq 1, \quad (14)$$

generated from the system in (6). The choice of Γ depends on the underlying dynamics and will be discussed in Section 3.3. For example, if the deterministic system has an attracting limit cycle, an appropriate choice is a single trajectory lying on that cycle; if it has multiple stable equilibria, Γ may consist of trajectories converging to each equilibrium.

We find an appropriate metric d to measure the distance between \mathbf{X} and points on the trajectories in Γ . Based on metric d , we identify the point $G(\mathbf{X}) \in \Gamma$ that is closest to \mathbf{X} . The phase of \mathbf{X} is the time coordinate $s \geq 0$ of this closest point. Formally, the phase s of \mathbf{X} is defined via

$$(j, s) = \operatorname{argmin}_{\ell \in \mathcal{L}, t \geq 0} d(\mathbf{X}, \mathbf{x}^{(\ell)}(t)), \quad \mathcal{L} = \{1, \dots, L\}, \quad (15)$$

and the associated reference point is obtained through the map $G : \mathbb{R}^n \rightarrow \Gamma$,

$$G(\mathbf{X}) = \mathbf{x}^{(j)}(s). \quad (16)$$

The most appropriate metric d to be used for the phase definition above depends on the system dynamics and will be discussed in Section 3.3. Aside from the phase-defining metric d and the reference trajectories Γ that are specific to the system dynamics, this definition of phase applies to any type of dynamics, not only oscillatory or multistable systems.

While the LNA is accurate for systems with linear dynamics (see Section 2.3.1), for systems with non-linear dynamics (e.g. oscillatory or multi-stable), as t increases the phase of $\mathbf{X}(t)$ will likely be very different to t . This means, with high probability, there exists some time point $\tau > 0$ such that $\mathbf{X}(\tau)$ is at a very different stage of its dynamic process to the deterministic $\mathbf{x}(\tau)$ despite $\mathbf{X}(0) = \mathbf{x}(0)$. Since the drift and diffusion in equation (9) which control the dynamics of $\mathbf{X}(t)$ for $t \geq \tau$ under the LNA depends only on $\mathbf{x}(t)$, the LNA will make predictions of $\mathbf{X}(t)$ for $t \geq \tau$ as if its in the same stage of its dynamic process as $\mathbf{x}(t)$ rather than considering the location of $\mathbf{X}(t)$. This leads to the LNA failing to capture the SSA dynamics of the reaction network $\{\mathbf{Y}(t)/\Omega : t \geq 0\}$ where $\{\mathbf{Y}(t) : t \geq 0\}$ evolves according to (4). We call this phenomenon a phase drift.

Therefore, initialising the LNA to the correct phase is a necessary condition for the LNA to be accurate for non-linear systems. This leads us to speculate that, if one can continually initialise the LNA with the correct phase so that the phase of the stochastic and deterministic trajectories remain in agreement, then the LNA will remain accurate at all times and produce paths agreeing with those from the SSA. We argue that, for some classes of dynamical systems, this is indeed the case. For instance, it is shown in [46] that this is true for systems whose RRE has an attractive limit cycle solution and a range of moderate system sizes.

This is the basis of the simulation algorithm developed next. We adopt the term used in [46] to name this simulation algorithm, phase corrected Linear Noise Approximation (pcLNA).

3.2 The pcLNA algorithm

Here we present the phase corrected Linear Noise Approximation (LNA) algorithm for simulating reaction networks with non-linear dynamics using LNA transitions. For each $t \geq 0$, we define the pcLNA ansatz;

$$\mathbf{X}(t) = \mathbf{x}(t) + \Omega^{-1/2} \boldsymbol{\xi}(t) = G(\mathbf{X}(t)) + \Omega^{-1/2} \boldsymbol{\kappa}(t). \quad (17)$$

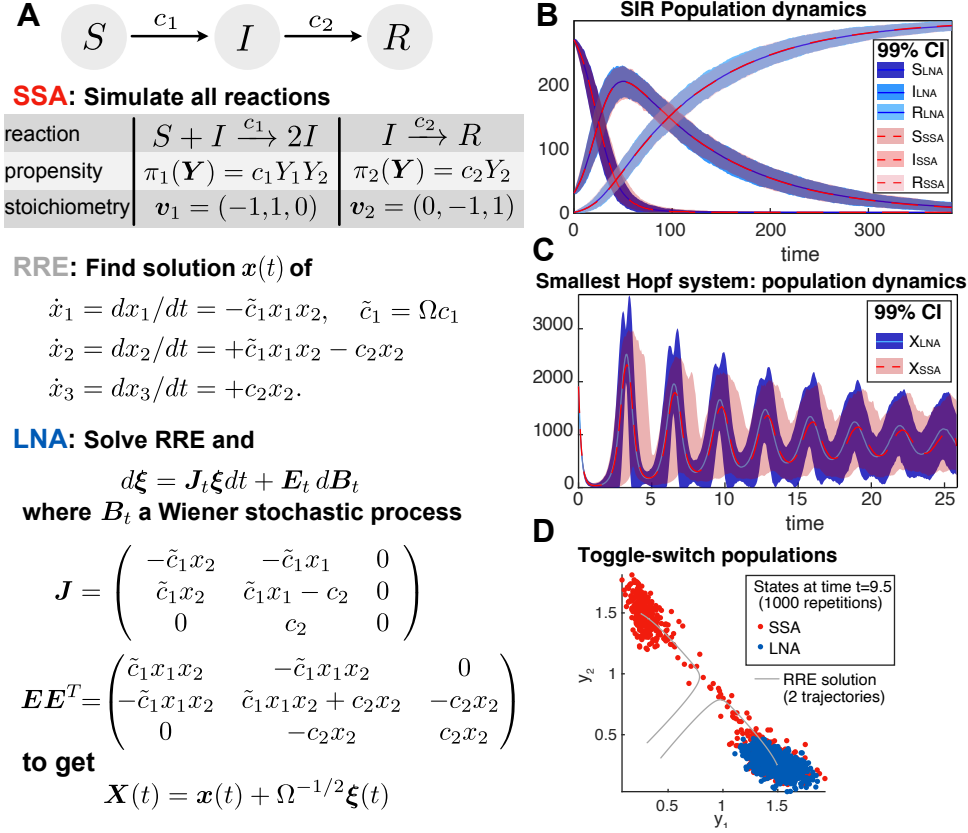


Figure 2: LNA method summary. A. LNA is a stochastic approximation of the stochastic population dynamics that can be exactly simulated using the SSA. LNA uses the numerical solutions of the deterministic RRE and a SDE that can be solved exactly. The SIR population dynamics model is used here as an example. B. Comparison between SSA and LNA on the SIR population dynamics in terms of simulated 99% Confidence Intervals (CI) shows astonishing agreement as the blue lines and shades almost completely overlap with the pink lines and shades. C. In contrast, same comparisons between the LNA and SSA in one of the three species of the oscillatory system in [71] show significant discrepancies. D. Significant discrepancies are also observed for the same comparisons on the bistable Genetic Toggle-Switch system in [14].

Here $G : \mathbb{R}^n \rightarrow \Gamma$, is the phase-correcting function (16) that maps any stochastic state $\mathbf{X}(t) \in \mathbb{R}^n$ to a point lying on a solution in some set of reference RRE solutions $\Gamma = \bigcup_{\ell=1}^L \{\mathbf{x}^{(\ell)}(t) : t \geq 0\}$ with its corresponding time being the phase $s \geq 0$ of the stochastic state $\mathbf{X}(t)$. The term $\boldsymbol{\kappa}(t)$ denotes the deviation of $\mathbf{X}(t)$ away from $G(\mathbf{X}(t))$ scaled by $\Omega^{-1/2}$. We use this ansatz to simulate stochastic trajectories as described in Algorithm 1.

The Algorithm 1 uses the standard LNA transition in steps 1-2 interrupted by phase-correcting maps in steps 3-4. The map G is used to find the phase for $\mathbf{X}(t_i)$. After phase correction, the phase of the system is moved from $s_{i-1} + \Delta t$ to s_i , the deterministic state moved from $\mathbf{x}^{(j_{i-1})}(s_{i-1} + \Delta t)$ to $\mathbf{x}^{(j_i)}(s_i)$ and the fluctuations $\boldsymbol{\xi}(s_{i-1} + \Delta t)$ are replaced with the remaining fluctuations after phase correction, $\boldsymbol{\kappa}(s_i)$. Provided Δt is not too large, phase drifts occurring in the next LNA transition will be small. Indeed, $\{\boldsymbol{\kappa}(s_i) : i \in \mathbb{N}_0\}$ should have uni-

Algorithm 1 General pcLNA algorithm

Inputs:

- a. Initial conditions: $t_0 = 0$, $\mathbf{X}(0)$, $\mathbf{x}^{(\ell)}(0)$, $\ell = 1, \dots, L$. Parameters: Δt , Ω .
- b. Solutions $\Gamma = \bigcup_{\ell=1}^L \{\mathbf{x}^{(\ell)}(t) : t \geq 0\}$ of a RRE as in (6) and the corresponding solutions $\mathbf{C}^{(\ell)}$ and $\mathbf{D}^{(\ell)}$ of (12), (13), respectively.
- c. A metric d on \mathbb{R}^n for the phase-correcting map $G : \mathbb{R}^n \rightarrow \Gamma$ as in (15), (16).

Steps: Set (j_0, s_0) such that $G(\mathbf{X}(0)) = \mathbf{x}^{(j_0)}(s_0)$ and take $\boldsymbol{\kappa}(s_0) = \Omega^{1/2}(\mathbf{X}(0) - \mathbf{x}^{(j_0)}(s_0))$. Then, for $i = 1, 2, \dots$,

1. draw sample $\boldsymbol{\xi}(s_{i-1} + \Delta t)$ from the MVN distribution with mean $\mathbf{C}^{(j_{i-1})}(s_{i-1}, s_{i-1} + \Delta t)\boldsymbol{\kappa}(s_{i-1})$, and variance matrix $\mathbf{D}^{(j_{i-1})}(s_{i-1}, s_{i-1} + \Delta t)$;
2. compute $\mathbf{X}(t_i) = \mathbf{x}^{(j_{i-1})}(s_{i-1} + \Delta t) + \Omega^{-1/2}\boldsymbol{\xi}(s_{i-1} + \Delta t)$;
3. set (j_i, s_i) such that $G(\mathbf{X}(t_i)) = \mathbf{x}^{(j_i)}(s_i)$;
4. set $\boldsymbol{\kappa}(s_i) = \Omega^{1/2}(\mathbf{X}(t_i) - \mathbf{x}^{(j_i)}(s_i))$.

Outputs: $\{\mathbf{X}(t_i) : i = 0, 1, 2, \dots\}$.

formly bounded variance and remain sufficiently small for the LNA predictions to be valid over the short time intervals $[s_i, s_i + \Delta t)$, $i \in \mathbb{N}_0$. Important for computational efficiency is that the same solutions of ODEs (6), (12) and (13) are used in all steps. The fact that these ODEs only need to be solved once before any simulations, rapidly increases the computation speed. The steps are illustrated in Figure 3.

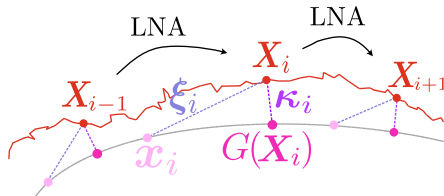


Figure 3: General pcLNA algorithm over steps $i - 1, i, i + 1$. For simplicity we illustrate the case where $j - 1 = j = j + 1$, so the same RRE solution is used over these steps. pcLNA proceeds with standard LNA steps interrupted by phase corrections with $\mathbf{x}^{(j_i)}(t_i)$ replaced by $G(\mathbf{X}(t_i)) = \mathbf{x}^{(j_i)}(s_i)$, and the perturbations $\boldsymbol{\xi}(t_i)$ replaced by $\boldsymbol{\kappa}(s_i)$.

All that is preventing one from readily applying the steps in the pcLNA algorithm is an explicit phase-defining metric d and a set of reference trajectories Γ used in the phase-correcting map G as in (15), (16). A natural question arises: does there exist a single choice of metric d and reference set Γ that can be used for all reaction networks to produce accurate simulations over long times? As we will explain, the answer is no. Phase depends on the system's underlying dynamics, and in particular on which components generate persistent non-linear behavior. Consequently, no universal metric can correctly capture phase across qualitatively different systems.

In the next section, we show how tools from dynamical systems theory provide a way to determine a phase-defining metric d and the set of reference trajectories Γ tailored to the system's qualitative dynamics.

3.3 Choosing the phase-defining metric d and set of reference trajectories Γ

We use three connected concepts from the dynamical systems theory to guide our approach in choosing metric d and set Γ used in the phase-correcting map G . The first concept is topological equivalence, which allows us to group systems exhibiting qualitatively identical dynamics. The second concept is decomposition, enabling us to break down complex (potentially high-dimensional) systems into a (possibly low-dimensional) non-linear component with persistent dynamics and components with transient dynamics. The third concept involves exemplar systems within each group that are well understood and can serve as references. We highlight the aspects of these concepts that are used in our approach in Sections 3.3.1, 3.3.2 and 3.3.3 and explain how we practically apply them in the construction of suitable metric d and set Γ in Section 3.3.4. We will then use this approach in Sections 4 and 5 to define d and Γ for systems presenting a Hopf bifurcation and a different d and Γ for systems exhibiting bistability through a fold bifurcation.

3.3.1 Topological equivalence

Two continuous dynamical systems of the form (6) are topologically equivalent if their dynamics are qualitatively identical. Formally, this holds if there exists a homeomorphism \mathbf{h} which maps paths of one system onto paths of the other while preserving the direction of time. Local topological equivalence (l.t.e.) occurs when this holds in neighborhoods of the systems' domains (see Definitions 2.14-5 in [37], or SI Section S3).

A practical approach to identify l.t.e. is to examine the eigenvalues of the Jacobian in (7) near an equilibrium point $(\mathbf{x}_{\alpha_p}, \alpha_p)$, with $\mathbf{F}(\mathbf{x}_{\alpha_p}, \alpha_p) = \mathbf{0}$. Let n_0 , n_+ , and n_- be the number of eigenvalues of $\mathbf{J}(\mathbf{x}_{\alpha_p}, \alpha_p)$ that have zero, positive, and negative real part, respectively. An equilibrium is hyperbolic if $n_0 = 0$; otherwise, it is non-hyperbolic. For hyperbolic equilibria, l.t.e. is ensured if n_+ and n_- match between systems (see Theorem 2.2 in [37]); the non-hyperbolic case is more subtle and discussed below.

3.3.2 Decomposition

Here we derive a novel decomposition of a stochastic process following the LNA to coordinates with different type of dynamics using results from the centre manifold theory (see [37, 59, 62, 51]), and Ito's differential calculus (see [38]). For a detailed description of the results used in this section and the calculations performed see SI Section S3.

Suppose the system (6) exhibits an equilibrium $(\mathbf{x}_\alpha, \alpha)$ which is non-hyperbolic ($n_0 > 0$) when $\alpha = \alpha_p$. In this setting, the system's non-linear dynamics can be reduced to occur on an α -dependent n_0 -dimensional *centre manifold* tangent to the eigenspace corresponding to the eigenvalues of $\mathbf{J}(\mathbf{x}_{\alpha_p}, \alpha_p)$ with zero real part (see Theorem 5.1 and Lemma 5.1 in [37]).

In fact, the system is l.t.e. to

$$\begin{cases} \dot{\mathbf{u}} = \mathbf{f}(\mathbf{u}, \alpha), \\ \dot{\mathbf{v}} = \mathbf{A}_s(\mathbf{u}, \alpha)\mathbf{v}, \\ \dot{\mathbf{w}} = \mathbf{A}_u(\mathbf{u}, \alpha)\mathbf{w}, \end{cases} \quad (18)$$

for paths and parameter values near to $(\mathbf{x}_{\alpha_p}, \alpha_p)$ where for each $t \geq 0$, $\mathbf{u}(t) \in \mathbb{R}^{n_0}$, $\mathbf{v}(t) \in \mathbb{R}^{n_-}$, $\mathbf{w}(t) \in \mathbb{R}^{n_+}$, $f : \mathbb{R}^{n_0} \times \mathbb{R} \rightarrow \mathbb{R}^{n_0}$ is smooth, $\mathbf{A}_s(\mathbf{u}(t), \alpha)$ is an $n_- \times n_-$ (stable) matrix with all of its eigenvalues having negative real part, and $\mathbf{A}_u(\mathbf{u}(t), \alpha)$ is an $n_+ \times n_+$ (unstable) matrix with all of its eigenvalues having positive real part (See Section 4 in [62] or Section 2 in [51]). Moreover, if the respective local homeomorphism denoted by $\mathbf{h}_\alpha : \mathbb{R}^n \rightarrow \mathbb{R}^n$ satisfies a set of generic nonresonance conditions of the eigenvalues of $\mathbf{J}(\mathbf{x}_{\alpha_p}, \alpha_p)$ that hold almost surely (see SI,

S3), \mathbf{h}_α is at least twice differentiable in a neighborhood of \mathbf{x}_{α_p} . In this setting, Itô's lemma (see [38, Theorem 5.10]) can be applied locally to characterise the image of the LNA under \mathbf{h}_α :

$$\begin{pmatrix} \mathbf{U}(t) \\ \mathbf{V}(t) \\ \mathbf{W}(t) \end{pmatrix} := \mathbf{h}_\alpha(\mathbf{x}(t) + \Omega^{-1/2}\boldsymbol{\xi}(t)) = \begin{pmatrix} \mathbf{u}(t) \\ \mathbf{v}(t) \\ \mathbf{w}(t) \end{pmatrix} + \Omega^{-1/2} \begin{pmatrix} \boldsymbol{\xi}_u(t) \\ \boldsymbol{\xi}_v(t) \\ \boldsymbol{\xi}_w(t) \end{pmatrix} + O(\Omega^{-1}), \quad (19)$$

for times $t \geq 0$ where $\mathbf{x}(t) + \Omega^{-1/2}\boldsymbol{\xi}(t)$ remains close to \mathbf{x}_{α_p} . Here $(\mathbf{u}(t), \mathbf{v}(t), \mathbf{w}(t))^\top := \mathbf{h}_\alpha(\mathbf{x}(t))$ evolves according to (18) and the perturbation $\tilde{\boldsymbol{\xi}}(t) = (\boldsymbol{\xi}_u(t), \boldsymbol{\xi}_v(t), \boldsymbol{\xi}_w(t))^\top$ evolves according to the system of SDEs

$$d\tilde{\boldsymbol{\xi}} = \tilde{\mathbf{J}}_t \tilde{\boldsymbol{\xi}} dt + \tilde{\mathbf{E}}_t dB_t \quad (20)$$

where

$$\tilde{\mathbf{J}}_t = \begin{bmatrix} \nabla_{\mathbf{u}} \mathbf{f}(\mathbf{u}, \alpha) & 0 & 0 \\ \nabla_{\mathbf{u}} (\mathbf{A}_s(\mathbf{u}, \alpha) \mathbf{v}) & \mathbf{A}_s(\mathbf{u}, \alpha) & 0 \\ \nabla_{\mathbf{u}} (\mathbf{A}_u(\mathbf{u}, \alpha) \mathbf{w}) & 0 & \mathbf{A}_u(\mathbf{u}, \alpha) \end{bmatrix}, \quad \tilde{\mathbf{E}}_t = \nabla_{\mathbf{x}} \mathbf{h}_\alpha(\mathbf{x}(t)) \mathbf{E}_t \quad (21)$$

Importantly under this local homeomorphism, the LNA, omitting $O(\Omega^{-1})$ terms, can be decomposed into 3 processes:

1. $\mathbf{U}(t) \approx \mathbf{u}(t) + \Omega^{-1/2}\boldsymbol{\xi}_u(t)$ the sum of a non-linear deterministic process, and a stochastic process with drift $\nabla_{\mathbf{u}} \mathbf{f}(\mathbf{u}, \alpha) \boldsymbol{\xi}_u$;
2. $\mathbf{V}(t) \approx \mathbf{v}(t) + \Omega^{-1/2}\boldsymbol{\xi}_v(t)$ the sum of an exponentially decaying deterministic process and a linear stochastic process with stable drift matrix,
3. $\mathbf{W}(t) \approx \mathbf{w}(t) + \Omega^{-1/2}\boldsymbol{\xi}_w(t)$ the sum of an exponentially growing deterministic process and a linear stochastic process with unstable drift matrix.

That is, at the $O(\Omega^{-1/2})$ scale, $\mathbf{V}(t)$ quickly drifts toward zero and $\mathbf{W}(t)$ quickly drifts outside the neighborhood, leaving all the effective stochastic behavior of the LNA to be described by $\mathbf{U}(t)$. This implies that any phase drift responsible for the long-term failure of the LNA arises from the dynamics of $\mathbf{U}(t)$ relative to $\mathbf{u}(t)$; the other processes, $\mathbf{V}(t)$ and $\mathbf{W}(t)$, play no long-term role and do not contribute to persistent phase drift.

Throughout the rest of the paper, we refer to the first n_0 coordinates of the image of \mathbf{h}_α , where $\mathbf{U}(t)$ and $\mathbf{u}(t)$ evolve, as the *centre coordinates*; the next n_- coordinates, where $\mathbf{V}(t)$ and $\mathbf{v}(t)$ evolve, as the *stable coordinates*; and last n_+ coordinates, where $\mathbf{W}(t)$ and $\mathbf{w}(t)$ evolve, as the *unstable coordinates*.

While this mapping is generally non-linear, its action on the *centre coordinates* admits a first-order approximation near the equilibrium (See SI Section S3). Specifically, for any point \mathbf{X} sufficiently close to \mathbf{x}_{α_p} , its location \mathbf{U} in the centre coordinates of $\mathbf{h}_\alpha(\mathbf{X})$ satisfies

$$\mathbf{U} = \mathbf{P}_c(\mathbf{X} - \mathbf{x}_{\alpha_p}) + O(\|\mathbf{X} - \mathbf{x}_{\alpha_p}\|^2), \quad (22)$$

where \mathbf{P}_c denotes the projection onto the eigenspace of $\mathbf{J}(\mathbf{x}_{\alpha_p}, \alpha_p)$ corresponding to eigenvalues of zero real part. It is important to note this is a first-order approximation of these coordinates and valid only sufficiently close to the equilibrium. Consequently, given a realization of the LNA, $\mathbf{X}(t) = \mathbf{x}(t) + \Omega^{-1/2}\boldsymbol{\xi}(t)$, the locations of $\mathbf{U}(t)$ are approximately

$$\mathbf{U}(t) \approx \mathbf{P}_c(\mathbf{X}(t) - \mathbf{x}_{\alpha_p}), \quad (23)$$

where $\mathbf{P}_c = \mathbf{R}_c^{-1}$ and \mathbf{R}_c is the $n \times n_0$ matrix whose columns form an eigenbasis corresponding to the eigenvalues of $\mathbf{J}(\mathbf{x}_{\alpha_p}, \alpha_p)$ with zero real part. Similarly,

$$\mathbf{u}(t) \approx \mathbf{P}_c(\mathbf{x}(t) - \mathbf{x}_{\alpha_p}). \quad (24)$$

3.3.3 Normal forms

Normal forms are simple exemplar systems representing classes of l.t.e. systems. Low-dimensional centre manifolds have well-studied normal forms, including the fold and Hopf bifurcations (see [37], Figure 4). We use normal forms in two ways. First, to specify the conditions under which a given system is l.t.e. to the normal form, typically related to the eigen-decomposition of the Jacobian. Secondly, we use their simpler form to identify the key qualitative features (e.g., oscillations, multi-stability) shared by systems in their class, guiding the choice of an appropriate metric d and set Γ for the phase-correcting map G .

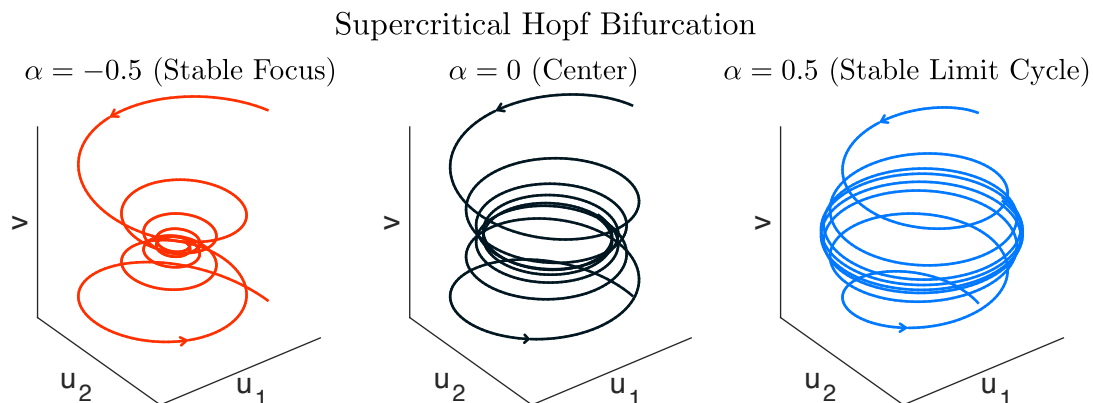


Figure 4: The dynamics of a generic normal form of the supercritical Hopf bifurcation. The two-dimensional centre manifold has coordinate $\mathbf{u} = (u_1, u_2)$, while the third coordinate v satisfies $\dot{v} = -v$. Selected orbits for the three different cases are presented.

3.3.4 Procedure for constructing the phase-correcting map

The theory in Sections 3.3.1-3.3.3 lead us to the following principles for defining the phase-defining metric d and set of reference trajectories Γ :

- A. Local topological equivalence (l.t.e.) identifies classes of systems whose trajectories are qualitatively identical near equilibria allowing the same construction of the phase-defining metric d and reference set Γ to be applied across all systems in the class.
- B. Decomposition isolates the coordinates in which non-linear, persistent dynamics — and hence phase drifts — occur. Phase and phase correction is defined exclusively in these centre coordinates, while the transient dynamics of the stable and unstable coordinates are disregarded when constructing the metric d .
- C. Normal forms provide canonical low-dimensional representatives of each l.t.e. class and make explicit the geometric structure of trajectories in the centre coordinates. This structure determines both the appropriate phase-defining metric and the choice of representative reference trajectories Γ .

Using these principles we define a procedure for constructing the phase-correcting map G for any system as in (6).

1. Check if there exists a parameter value α_p and a state \mathbf{x}_{α_p} in a neighborhood of interest such that $\mathbf{F}(\mathbf{x}_{\alpha_p}, \alpha_p) = \mathbf{0}$, and the Jacobian $\mathbf{J}(\mathbf{x}_{\alpha_p}, \alpha_p)$ has $n_0 > 0$ eigenvalues with zero

real part. If so, proceed to the next step; otherwise, consider using an alternative method (including the standard LNA).

2. Identify the local topological equivalence (l.t.e.) class of (6) by checking whether it satisfies the conditions of a known normal form, such as those associated with Hopf bifurcations or bi-stable systems (see Sections 4 and 5).
3. Based on the l.t.e. class dynamics and, where applicable, the corresponding normal form, choose a set of reference trajectories $\Gamma = \bigcup_{\ell=1}^L \{\mathbf{x}^{(\ell)}(t) : t \geq 0\}$, containing at least one deterministic solution of each distinct type of qualitative behaviour. For example, if the system admits three stable equilibria, select three trajectories converging to each equilibrium.
4. Define a projection map to find the approximate location of a point near \mathbf{x}_{α_p} in the centre coordinates:

$$\text{proj} : \mathbb{R}^n \rightarrow \mathbb{R}^{n_0}, \quad \text{proj}(\mathbf{x}) = \mathbf{R}_c^{-1}(\mathbf{x} - \mathbf{x}_{\alpha_p}), \quad (25)$$

where \mathbf{R}_c is an $n \times n_0$ matrix whose columns form an eigenbasis corresponding to the eigenvalues of $\mathbf{J}(\mathbf{x}_{\alpha_p}, \alpha_p)$ that have zero real part.

5. Compute the projections of all reference trajectories

$$\{\mathbf{u}^{(\ell)}(t) = \text{proj}(\mathbf{x}^{(\ell)}(t)) : t \geq 0\}, \quad \ell \in \mathcal{L}, \quad \mathcal{L} = \{1, \dots, L\} \quad (26)$$

and, for any stochastic state $\mathbf{X} \in \mathbb{R}^n$, define

$$\mathbf{U} := \text{proj}(\mathbf{X}). \quad (27)$$

6. Define the distance metric $d : \mathbb{R}^n \times \mathbb{R}^n \rightarrow [0, \infty)$, by

$$d(\mathbf{y}, \mathbf{x}) := \|\text{proj}(\mathbf{y}) - \text{proj}(\mathbf{x})\|. \quad (28)$$

7. Using (25)-(28), the phase-correcting map $G : \mathbb{R}^n \rightarrow \Gamma$ defined in (15) is given by

$$G(\mathbf{X}) = \mathbf{x}^{(j)}(s), \quad \text{where } (j, s) = \underset{\ell \in \mathcal{L}, t \geq 0}{\text{argmin}} d(\mathbf{X}, \mathbf{x}^{(\ell)}(t)) = \underset{\ell \in \mathcal{L}, t \geq 0}{\text{argmin}} \|\mathbf{U} - \mathbf{u}^{(\ell)}(t)\|. \quad (29)$$

In summary, this procedure defines the phase-correcting function G , which maps any stochastic state \mathbf{X} to the point on the reference trajectories in Γ that is closest to \mathbf{X} in the approximate centre coordinates. Figure 5 illustrates steps (5-8) above.

Although the true centre coordinates are given by the α -dependent map \mathbf{h}_α , the linear projection (25) provides a first-order approximation that is independent of α and can therefore be used consistently across parameter values.

For the numerical investigations in Section 6, we use the Euclidean norm (28), though other metrics may be employed.

In Section 4 and 5 we apply this procedure for two concrete types of dynamics: Oscillations (sustained or damped) and bistability which occur when the RRE in (6) contains a Hopf bifurcation and generic fold bifurcation respectively. We show the resulting metrics d and sets Γ can be used to accurately simulate such dynamics in Section 6.

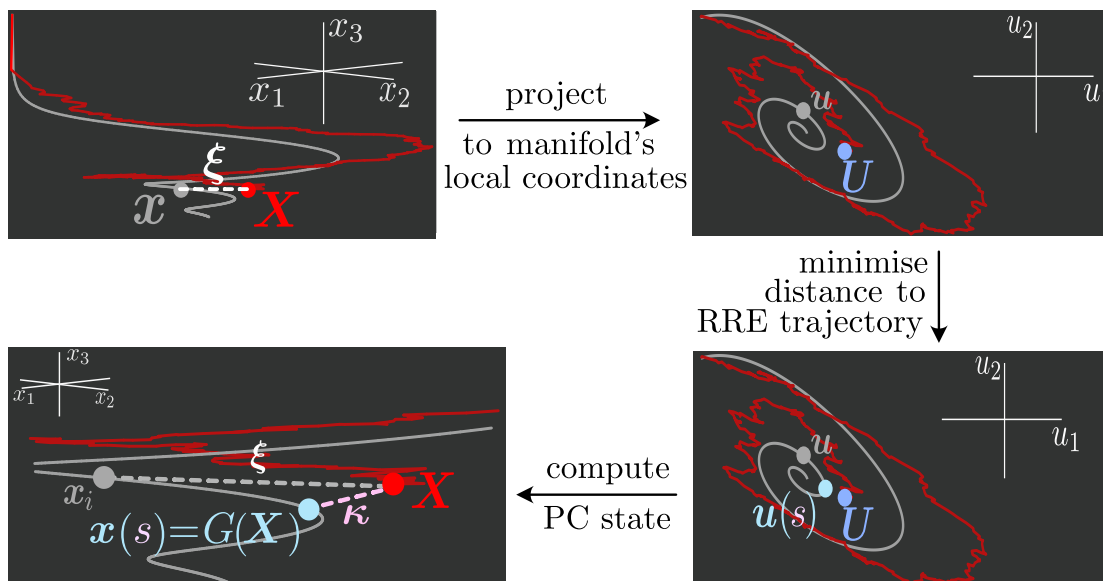


Figure 5: Phase correction. The phase-correcting map $G(\mathbf{X}_i)$ for a point \mathbf{X}_i on the stochastic trajectory is computed in three steps. First, the RRE solution and point \mathbf{X}_i is projected into the centre coordinates of the non-linear Centre manifold. Then, the point, $\mathbf{u}(s_i)$ lying on the projected RRE trajectory $\{\mathbf{u}(t) : t \geq 0\}$ that minimises the distance to \mathbf{U}_i is found. Finally, the corresponding point, $\mathbf{x}(s_i)$, with the same time-point s_i with $\mathbf{u}(s_i)$ and that lies on the RRE solution $\{\mathbf{x}(t) : t \geq 0\}$ is found. The point $\mathbf{x}(s_i)$ and the perturbation $\boldsymbol{\kappa}_i$ (instead of \mathbf{x}_i and $\boldsymbol{\xi}_i$) are used in the next LNA transition. The magnitude of $\boldsymbol{\kappa}_i$ is smaller than or equal to the magnitude of $\boldsymbol{\xi}_i$ on the centre coordinates.

4 Hopf bifurcation systems

We now consider systems which present oscillatory behaviour. In particular, we wish to draw a stochastic trajectory $\{\mathbf{X}(t_i) : i = 0, 1, 2, \dots\}$, with $\mathbf{X}(t_i) \in \mathbb{R}^n$ for a reaction network with macroscopic RRE as in (6) and Jacobian $\mathbf{J}(\mathbf{x}, \alpha)$ as in (7) that satisfy the following conditions:

- (H.I) there exists an $\alpha_p \in \mathbb{R}$ and $\mathbf{x}_{\alpha_p} \in \mathbb{R}^n$ such that, $\mathbf{F}(\mathbf{x}_{\alpha_p}, \alpha_p) = \mathbf{0}$,
- (H.II) for α local to α_p , all the eigenvalues of the Jacobian matrix, $\mathbf{J}(\mathbf{x}_{\alpha}, \alpha)$ are negative except for a pair of complex conjugate eigenvalues $\lambda(\alpha)$, $\bar{\lambda}(\alpha)$ such that

$$\lambda(\alpha) = \mu(\alpha) + i\omega(\alpha), \quad \text{where } \mu(\alpha_p) = 0, \omega(\alpha_p) > 0.$$

Condition (H.I) is precisely the requirement for the macroscopic reaction rate equation to exhibit an equilibrium. Condition (H.II) ensures the equilibrium is non-hyperbolic and therefore prescribes the existence of a parameter dependent, two-dimensional, attracting manifold near $(\mathbf{x}_{\alpha_p}, \alpha_p)$ for which (6) is l.t.e. to a system

$$\begin{cases} \dot{\mathbf{u}} = \mathbf{f}(\mathbf{u}, \alpha), \\ \dot{\mathbf{v}} = \mathbf{A}(\mathbf{u}, \alpha)\mathbf{v}, \end{cases} \quad (30)$$

where for each $t \geq 0$, $\mathbf{u}(t) \in \mathbb{R}^2$, $\mathbf{v}(t) \in \mathbb{R}^{n-2}$, $\cdot : \mathbb{R}^2 \times \mathbb{R} \rightarrow \mathbb{R}^2$ is smooth and $\mathbf{A}(\mathbf{u}(t), \alpha)$ is an $(n-2) \times (n-2)$ matrix with all of its eigenvalues having negative real part. See Figure 4 for an illustration of the paths of the normal form of this system.

Since all the eigenvalues other than the complex pair have negative real values, then the calculations in Section 3.3.2 reveal the image of the LNA, $\mathbf{X}(t) = \mathbf{x}(t) + \Omega^{-1/2}\boldsymbol{\xi}(t)$, under the local homeomorphism reveals two stochastic processes: $\mathbf{U}(t) \approx \mathbf{u}(t) + \Omega^{-1/2}\boldsymbol{\xi}_u(t)$, evolving in the centre coordinates and exhibiting the non-linear dynamics; and $\mathbf{V}(t) \approx \mathbf{v}(t) + \Omega^{-1/2}\boldsymbol{\xi}_v(t)$, evolving in the stable coordinates and decaying at an exponential rate. Their stochastic perturbations, $\boldsymbol{\xi}_u(t)$ and $\boldsymbol{\xi}_v(t)$, evolve according to (20).

4.1 The pcLNA algorithm for Hopf bifurcation systems

For a reaction network with macroscopic RRE as in (6) satisfying conditions (H.I), (H.II), we now wish to define the projection metric d and set of reference trajectories Γ to define the phase-correcting map G , as described in Section 3.3.4. Consider some value α of the bifurcation parameter that is near the critical α_p . The normal form dynamics imply that trajectories starting from different initial conditions rapidly converge to a common path. This motivates the use of a single deterministic trajectory $\Gamma = \{\mathbf{x}(t) : t \geq 0\}$ near \mathbf{x}_{α_p} , which proved sufficient to achieve accurate simulations for all systems considered in Section 6.

To obtain a readily applicable G using the steps in Section 3.3.4 we identify the conjugate pair of eigenvectors, $\hat{\mathbf{u}}_1 \pm i\hat{\mathbf{u}}_2$, corresponding to the imaginary eigenvalues of the Jacobian $\mathbf{J}(\mathbf{x}_{\alpha_p}, \alpha_p)$ as in (H.II). Then, the eigenspace corresponding to these complex eigenvalues is spanned by $\{\hat{\mathbf{u}}_1, \hat{\mathbf{u}}_2\}$. Letting $\mathbf{R}_c = [\hat{\mathbf{u}}_1 \ \hat{\mathbf{u}}_2]$ we define the map $\text{proj} : \mathbb{R}^n \rightarrow \mathbb{R}^2$, $\text{proj}(\mathbf{x}) = \mathbf{R}_c^{-1}(\mathbf{x} - \mathbf{x}_{\alpha_p})$. Now d and G can be defined as in (28), and (29) with $L = 1$; phase correction occurs to minimize the distance in the approximate centre coordinates between the stochastic state $\mathbf{U} = \text{proj}(\mathbf{X})$ and single deterministic path $\{\mathbf{u}(t) = \text{proj}(\mathbf{x}(t)) : t \geq 0\}$. Having defined the metric d for the map G , one may follow the steps in Algorithm 1 to produce simulations of Hopf bifurcation systems.

Since only one RRE solution Γ is required for this type of system the map G can be written as the convolution $G = \mathbf{x} \circ \mathcal{M} \circ \text{proj}$ where $\mathcal{M} : \mathbb{R}^2 \rightarrow [0, \infty)$, such that $s = \mathcal{M}(\mathbf{U}) = \text{argmin}_{t \geq 0} \|\mathbf{U} - \mathbf{u}(t)\|$ (see Figure 6). For ease, we provide a pcLNA algorithm specifically for Hopf bifurcation systems using this notation in Algorithm 2. In Section 6, we show that this algorithm is sufficient to achieve high levels of accuracy.

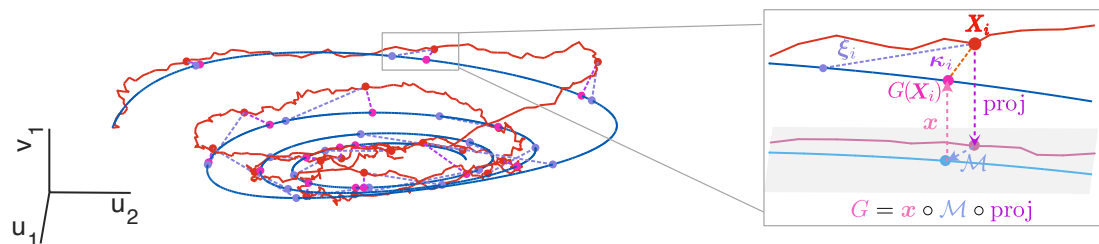


Figure 6: Phase correction (PC) for Hopf bifurcation systems. (Left) The stochastic trajectory (red) and deterministic trajectory (blue) in coordinates (\mathbf{u}, v_1) are displayed. The stochastic state (red circle) and the perturbations before ($\boldsymbol{\xi}$, purple, dashed line) and after ($\boldsymbol{\kappa}$, pink, dashed line) PC are displayed. (Right) Zoom in of a PC with the G map analysed as a convolution of the projection (proj), distance minimisation (\mathcal{M}), and lift back to original coordinates (\mathbf{x}) functions.

Algorithm 2 pcLNA for Hopf bifurcation systems

Inputs:

- a. Initial conditions: $t_0 = 0$, $\mathbf{x}(0)$, $\mathbf{X}(0)$, Parameters: Δt , Ω .
 - b. System satisfying (H.I), (H.II), with solution $\Gamma = \{\mathbf{x}(t) : t \geq 0\}$ of (6) and the corresponding solutions \mathbf{C} and \mathbf{D} of (12), (13), respectively.
 - c. The projection map $\text{proj} : \mathbb{R}^n \rightarrow \mathbb{R}^2$, $\text{proj}(\mathbf{x}) = \mathbf{R}_c^{-1}(\mathbf{x} - \mathbf{x}_{\alpha_p})$ where $\mathbf{R}_c = [\hat{\mathbf{u}}_1 \ \hat{\mathbf{u}}_2]$ with $\hat{\mathbf{u}}_1, \hat{\mathbf{u}}_2$ an eigenbasis corresponding to the conjugate pair of imaginary eigenvalues of $\mathbf{J}(\mathbf{x}_{\alpha_p}, \alpha_p)$.
- Steps:** Compute $\{\mathbf{u}(t) : t \geq 0\}$, where $\mathbf{u}(t) = \text{proj}(\mathbf{x}(t))$ and set s_0 such that $G(\mathbf{X}(0)) = \mathbf{x}(s_0)$ with $\boldsymbol{\kappa}(s_0) = \Omega^{1/2}(\mathbf{X}(0) - \mathbf{x}(s_0))$.

For $i = 1, 2, \dots$,

1. draw sample $\boldsymbol{\xi}(s_{i-1} + \Delta t)$ from the MVN distribution with mean $\mathbf{C}(s_{i-1}, s_{i-1} + \Delta t)\boldsymbol{\kappa}(s_{i-1})$, and variance matrix $\mathbf{D}(s_{i-1}, s_{i-1} + \Delta t)$;
2. compute $\mathbf{X}(t_i) = \mathbf{x}(s_{i-1} + \Delta t) + \Omega^{-1/2}\boldsymbol{\xi}(s_{i-1} + \Delta t)$;
3. compute $\mathbf{U}_i = \text{proj}(\mathbf{X}(t_i))$, and find $s_i = \mathcal{M}(\mathbf{U}_i) = \text{argmin}_{t \geq 0} \|\mathbf{U}_i - \mathbf{u}(t)\|$.
4. compute $\boldsymbol{\kappa}(s_i) = \Omega^{1/2}(\mathbf{X}(t_i) - \mathbf{x}(s_i))$.

Outputs: $\{\mathbf{X}(t_i) : i = 0, 1, 2, \dots\}$.

5 Bi-stable systems

We now consider systems that present bi-stability and wish to derive stochastic trajectories $\{\mathbf{X}(t_i) : i = 0, 1, 2, \dots\}$, with $\mathbf{X}(t_i) \in \mathbb{R}^n$, for a reaction network with RRE limit (as $\Omega \rightarrow \infty$) satisfying (6) and Jacobian, $\mathbf{J}(\mathbf{x}, \alpha)$, as in (7) that satisfy the following conditions:

- (B.I) there exists an $\alpha_p \in \mathbb{R}$ and $\mathbf{x}_{\alpha_p} \in \mathbb{R}^n$ such that $\mathbf{F}(\mathbf{x}_{\alpha_p}, \alpha_p) = \mathbf{0}$;
- (B.II) all the eigenvalues of the Jacobian matrix $\mathbf{J}(\mathbf{x}_{\alpha_p}, \alpha_p)$ are negative except for one zero eigenvalue.
- (B.III) for α near $\alpha_p \in \mathbb{R}$ there exists $\mathbf{x}_*^{(1)} \in \mathbb{R}^n$ such that $\mathbf{F}(\mathbf{x}_*^{(1)}, \alpha) = \mathbf{0}$ and all the eigenvalues of the Jacobian matrix $\mathbf{J}(\mathbf{x}_*^{(1)}, \alpha)$ are negative.

The last condition (B.III) ensures the presence of a stable equilibrium point for all values of α near α_p . The conditions (B.I-II) prescribe the presence of a non-hyperbolic equilibrium, \mathbf{x}_{α_p} , and the existence of a parameter dependent, one-dimensional, attracting manifold near $(\mathbf{x}_{\alpha_p}, \alpha_p)$ for which (6) is l.t.e. to a system

$$\begin{cases} \dot{u} = f(u, \alpha), \\ \dot{\mathbf{v}} = \mathbf{A}(u, \alpha)\mathbf{v}, \end{cases} \quad (31)$$

where for each $t \geq 0$, $u(t) \in \mathbb{R}$, $\mathbf{v}(t) \in \mathbb{R}^{n-1}$, $f : \mathbb{R} \times \mathbb{R} \rightarrow \mathbb{R}$ is smooth and $\mathbf{A}(u(t), \alpha)$ is an $(n-1) \times (n-1)$ matrix with all of its eigenvalues having negative real part. For the generic fold bifurcation system (31), the non-hyperbolic equilibrium present at α_p disappears for $\alpha < \alpha_p$ while two equilibrium points, one stable and one unstable, emerge for $\alpha > \alpha_p$. Therefore, a system satisfying the conditions (B.I-III) presents two stable and one unstable equilibrium points for $\alpha > \alpha_p$. That is, we arrive to the following result.

Remark 1 (Bistability). For a system as in (6) satisfying the conditions (B.I)-(B.III), with value of α such that $\alpha - \alpha_p$ is positive and sufficiently small, there exist $\mathbf{x}_*^{(1)}, \mathbf{x}_\alpha, \mathbf{x}_*^{(2)} \in \mathbb{R}^n$

with $\mathbf{F}(\mathbf{x}_*^{(1)}, \alpha) = \mathbf{F}(\mathbf{x}_\alpha, \alpha) = \mathbf{F}(\mathbf{x}_*^{(2)}, \alpha) = \mathbf{0}$ and all the eigenvalues of the Jacobian matrices $\mathbf{J}(\mathbf{x}_*^{(1)}, \alpha)$ and $\mathbf{J}(\mathbf{x}_*^{(2)}, \alpha)$ are negative (linear stability), while $\mathbf{J}(\mathbf{x}_\alpha, \alpha)$ has one positive eigenvalue (instability) and the rest are negative.

Similarly to Hopf bifurcation systems in Section 4, the image of the LNA, $\mathbf{X}(t) = \mathbf{x}(t) + \Omega^{-1/2}\boldsymbol{\xi}(t)$ under the local homeomorphism reveals stochastic processes $U(t) \approx u(t) + \Omega^{-1/2}\xi_u(t)$, evolving in the single centre coordinate; and $\mathbf{V}(t) \approx \mathbf{v}(t) + \Omega^{-1/2}\boldsymbol{\xi}_v(t)$, evolving in the stable coordinates. Their stochastic perturbations, $\xi_u(t)$ and $\boldsymbol{\xi}_v(t)$, evolve according to (20).

5.1 The pcLNA algorithm for bi-stable systems

A system satisfying Remark 1 with $\alpha > \alpha_p$ exhibits two stable equilibrium points. The standard LNA, which relies on a single deterministic solution to simulate a trajectory, will produce paths centered around the “nearest” equilibrium. As a result, it will fail to approximate trajectories produced by the SSA whenever there is a substantial probability that a stochastic trajectory produced by the SSA escapes from this equilibrium (see Figure 2(D) and SI Figure S19).

Here we discuss how to choose a metric d and a set of reference trajectories Γ (following the procedure in 3.3.4) in order to apply the pcLNA algorithm in 1 and obtain accurate simulations.

If $\mathbf{R}_c = \mathbf{u}_1$ is the eigenvector corresponding to the zero eigenvalue of $\mathbf{J}(\mathbf{x}_{\alpha_p}, \alpha_p)$, then we define the projection map $\text{proj} : \mathbb{R}^n \rightarrow \mathbb{R}$, onto the eigenspace that assigns to each state \mathbf{x} its approximate location in the centre coordinate $u = \text{proj}(\mathbf{x}) = \mathbf{R}_c^{-1}(\mathbf{x} - \mathbf{x}_{\alpha_p})$. Again, the distance metric in (28) is $d(\mathbf{X}, \mathbf{x}) = |U - u|$, where $U = \text{proj}(\mathbf{X})$, and $u = \text{proj}(\mathbf{x})$.

When selecting the set of reference trajectories Γ , at least two trajectories—each converging to a different equilibrium—are required. This is necessary to allow stochastic trajectories that start from the same initial condition to reach the vicinity of different equilibria via LNA transitions, a behavior that is observed in SSA trajectories.

Having defined the distance metric d and the set of reference trajectories Γ , we can apply (15) and (16) to define the phase-correcting map G and therefore apply the Algorithm 1.

With this in place, we now present a pcLNA algorithm specifically for bistable systems in Algorithm 3. In Section 6, we show that this simple phase map is sufficient to achieve high levels of accuracy.

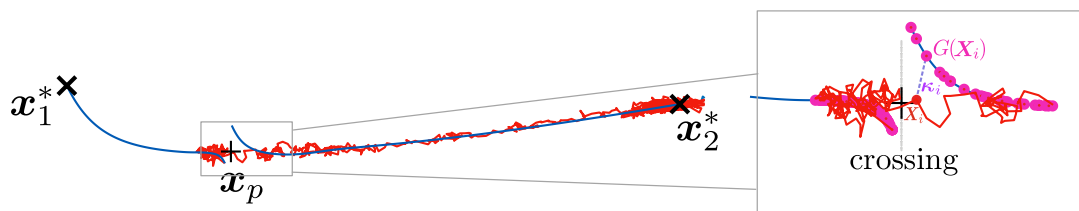


Figure 7: Phase Correction (PC) for bistable systems. (Left) The stochastic trajectory (red) and two deterministic trajectories (blue), each converging to a different stable equilibrium (\mathbf{x}) on the two sides of the unstable equilibrium (+) are displayed. (Right) Zoom in to the part of simulation where a crossing from one side of the unstable equilibrium to the other was performed with the PC mapping G (pink circles) and the deviation κ_i shown.

Algorithm 3 pcLNA for bistable systems

Inputs:

- a. Initial conditions: $s_0 = 0 = t_0$, $j_0 \in \{1, 2\}$, $\mathbf{X}(0)$, $\{\mathbf{x}^{(j)}(0) : j = 1, 2\}$. Parameters: Δt , Ω .
- b. System satisfying Remark 1 with solutions $\gamma_j = \{\mathbf{x}^{(j)}(t) : t \geq 0\}$ converging to \mathbf{x}_j^* , $j = 1, 2$, respectively, and their corresponding solutions $\mathbf{C}^{(j)}$ and $\mathbf{D}^{(j)}$ of (12), (13), respectively.
- c. The projection map $\text{proj} : \mathbb{R}^n \rightarrow \mathbb{R}$, $u = \text{proj}(\mathbf{x}) = \mathbf{R}_c^{-1}(\mathbf{x} - \mathbf{x}_{\alpha_p})$ where $\mathbf{R}_c = \mathbf{u}$ with \mathbf{u} a normalised eigenvector corresponding to the zero eigenvalue of $\mathbf{J}(\mathbf{x}_{\alpha_p}, \alpha_p)$.

Steps: Compute $\{u^{(j)}(t) : t \geq 0\}$ where $u^{(j)}(t) = \text{proj}(\mathbf{x}^{(j)}(t))$ for $j = 1, 2$, and $\boldsymbol{\kappa}(s_0) = \Omega^{1/2}(\mathbf{X}(0) - \mathbf{x}^{(j_0)}(0))$. For $i = 1, 2, \dots$

1. draw sample $\boldsymbol{\xi}(s_{i-1} + \Delta t)$ from the MVN distribution with mean $\mathbf{C}^{(j_{i-1})}(s_{i-1}, s_{i-1} + \Delta t)\boldsymbol{\kappa}(s_{i-1})$, and variance matrix $\mathbf{D}^{(j_{i-1})}(s_{i-1}, s_{i-1} + \Delta t)$;
2. compute $\mathbf{X}(t_i) = \mathbf{x}^{(j_{i-1})}(s_{i-1} + \Delta t) + \Omega^{-1/2}\boldsymbol{\xi}(s_{i-1} + \Delta t)$;
3. compute $U = \text{proj}(\mathbf{X}(t_i))$ and find $(j_i, s_i) = \text{argmin}_{\ell \in \{1, \dots, L\}, t \geq 0} \|U - u^{(\ell)}(t)\|$;
4. compute $\boldsymbol{\kappa}(s_i) = \Omega^{1/2}(\mathbf{X}(t_i) - \mathbf{x}^{(j_i)}(s_i))$.

Outputs: $\{\mathbf{X}(t_i) : i = 0, 1, 2, \dots\}$.

6 Numerical investigations

As mentioned in Section 2.3, the LNA boasts fast computation of distributions of the stochastic process $\{\mathbf{X}(t) : t \geq 0\}$ as it only demands solving a set of ODEs to derive the RRE solutions $\{\mathbf{x}^{(j)}(t) : t \geq 0\}$, $j = 1, \dots, J$ in (6) and the corresponding drift and diffusion matrix solutions, $\mathbf{C}^{(j)}$ and $\mathbf{D}^{(j)}$, of Eq. (12-13). Since the pcLNA algorithm also only requires such solutions, it also inherits its speed of simulation.

Next, we study the accuracy and computational efficiency of the pcLNA compared to the SSA. For this, we separately use SSA and pcLNA to produce a large number of long-time, stochastic trajectories and then compare their empirical probability distribution at various time-points. We perform this exercise for various systems, either presenting bi-stability or a Hopf bifurcation. All numerical investigations were performed on a MacBook Pro workstation with an Apple M2 processor (8 CPU cores) and 16 GB RAM using the software PeTTSy [10] in MATLAB. [27].

For Hopf bifurcation systems, we perform comparisons for all three qualitatively different cases where the system complex conjugate pair of eigenvalues in (H.II) has $\mu(\alpha) < 0, = 0, > 0$. In these three cases, the limiting RRE system presents quickly dampened oscillations with a focus shape, slowly dampened oscillations, and sustained oscillations, respectively (see also Figure 1A and 4). For bistable systems, we focus on parameter values satisfying 1 (see Figure 1B, right) where the system present bistability.

The Hopf bifurcation systems used for comparisons are the following.

- The Brusselator system in [39], which is a classical oscillatory system involving complex interactions between two variables (for more details, see SI Section S4.2).
- The three-variable system in [71] that is the smallest reaction network presenting a Hopf bifurcation (see SI Section S4.3).
- The response of the NF- κ B signalling system to TNF α signals in [4], which is a system that involves 11 molecular populations involved in 24 reactions (see SI Section S4.1).

For the first two systems above, we produced 1000 stochastic trajectories using SSA and pcLNA for a time interval with length of 8τ , where τ the length of one period-cycle of the corresponding system. For the third system (where SSA simulations are substantially slower), we run 500 repetitions for a time-length of 4 periods of the system. We recorded the time taken to compute one stochastic trajectory for these time intervals, and then computed the median of these times, which we call CPU time in all the presented figures. We also collected using these simulations the state, $(X_1(t_j), \dots, X_n(t_j))$ of all variables at various time-points, $t_j, j = 1, 2, \dots, T$ in each repetition, and computed the corresponding empirical density functions for the probability distribution of each variable $X_i(t_j)$ using kernel density estimation in MATLAB [27]. We present the results in Figure 8A and SI Figures S9- S17.

We clearly see that the pcLNA and SSA distributions are hardly distinguishable, while the CPU time is reduced by a magnitude of order $O(10) - O(10^3)$. The reduction in CPU time depends on the complexity of the system (number and speed of reactions) and the system size. Larger system sizes imply larger number of reaction occurrences and slower SSA simulations, while CPU times for pcLNA are not affected by system size.

The bi-stable systems considered are the following.

- The genetic toggle-switch system in [14], which involves two-variables (for more details, see SI Section S4.4).
- The two-variable, simplified cell-cycle system presented in [2] (see SI Section S4.5).
- The somitogenesis switch system, presented in [21], that involves four variables and ten reactions (see SI Section S4.6).

We produced 1000 trajectories using SSA and pcLNA for the above systems, running for time intervals of length sufficient for convergence to one of the two stable equilibria by the solution of the corresponding RRE.

Note that if we initialise the system at a point close to one of the stable equilibria, then nearly all trajectories converge to the same equilibrium and the SSA simulations are well approximated by the standard LNA. Instead, we focused on simulations where the initial conditions are close to the unstable equilibrium so that there is a substantial probability of convergence of a given stochastic trajectory for both equilibria. In this case, all the standard LNA trajectories will converge to the same equilibrium and therefore can badly fail to approximate the SSA simulations (see Figure 2(D) and SI Figure S19).

The pcLNA algorithm 3 requires the choice of at least two solutions of RRE that differ only by their initial condition and converge to a different equilibrium. In the presented simulations, the two initial conditions are of the form $(1 - \epsilon) \mathbf{x}_\alpha + \epsilon \mathbf{x}_*^{(j)} + \mathbf{c}, j = 1, 2$. Here $0 \leq \epsilon \leq 0.1$, \mathbf{x}_α the unstable equilibrium and $\mathbf{x}_*^{(j)}, j = 1, 2$, the stable equilibria. The real vector \mathbf{c} performs a change of location in a direction orthogonal to the eigenvector corresponding to the real positive eigenvalue of the Jacobian $\mathbf{J}(\mathbf{x}^u)$. This change of location allows to view some short-time transient dynamics, but it is not necessary if one is interested in the long-time dynamics. For the specific initial conditions and other details, see SI Sections S4.4-S4.6.

The results are presented in Figure 8B and SI Figures S18, S20, S21. The two methods, SSA and pcLNA, are compared in the same way as the Hopf bifurcation system and the results are again showing the agreement between the two methods and similarly to above, significant reductions in the CPU time, especially for the Somitogenesis Switch system (pcLNA CPU time is ≈ 58 times smaller).

Finally, to quantify the computational cost of SSA and pcLNA across systems, we report the CPU times in Table 1. We also introduce a simple and practical predictor of the SSA runtime based on the system's average reaction activity.

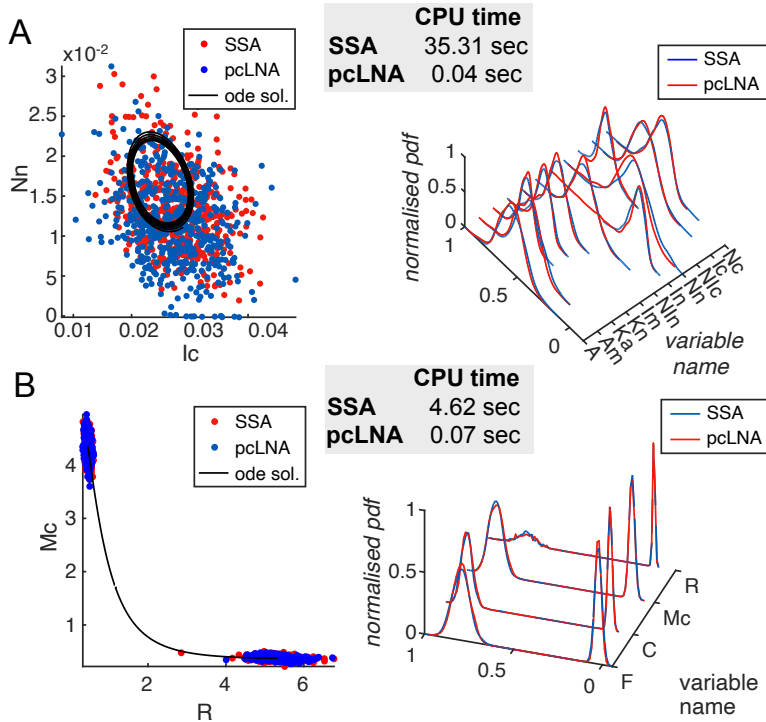


Figure 8: Comparison between SSA (red) and pcLNA (blue) for (A) the NF- κ B [4] and (B) the somitogenesis switch [21] system. (Left) The states recorded after four cycles (A) and at $t = 100$ mins (B) of respectively $n = 500$ and $n = 1000$ simulations of the two systems and solutions of the corresponding RRE in (6). (Right) The corresponding empirical probability density functions of each of the system variables. The median CPU times for deriving one stochastic trajectory are also reported. See SI Section S4 for the details of the simulations.

For a given system, the total propensity $\pi_0(\mathbf{Y}) = \sum_{j=1}^r \pi_j(\mathbf{Y})$, is evaluated along the deterministic trajectories $\{\mathbf{x}^{(\ell)}(t) : t \in [0, T], \ell \in \mathcal{L}\}$ used for pcLNA simulation taking $\mathbf{Y} = \Omega \mathbf{x}^{(\ell)}(t)$ (here $\mathcal{L} = \{1, \dots, L\}$, $L \in \{1, 2\}$). This yields the time-dependent reaction activity of the mean-field dynamics which, although it neglects stochastic deviations, provides a reliable summary of the system's reaction intensity over different dynamical phases. We then define the average total propensity

$$\bar{\pi}_0 = \int_0^T \pi_0(\Omega \mathbf{x}(t)) dt.$$

Since the SSA explicitly simulates every reaction event, and each event has constant computational cost, the expected number of reactions in time T , given by $N_r = T\bar{\pi}_0$, provides an easily-computable, interpretable predictor of SSA runtime.

For the systems in Table 1, this predictor correlates extremely strongly with the measured SSA CPU times ($\rho = 0.9963$). In contrast, we see that systems with similar number of reactions or number of populations have CPU times of different order of magnitude for both SSA and pcLNA. In the same table, we see that pcLNA runtime compared to SSA is orders of magnitude smaller and grow much more slowly with system complexity. For example, while SSA is $O(10^4)$ times slower for the NF- κ B model than for the toggle-switch system, pcLNA times are of the

same order.

System	$N_r/10^3$	n	r	CPU time	
				SSA	pcLNA
toggle-switch [14]	5.0347	2	4	0.0296	0.0110
cell-cycle [2]	4.4595	2	6	0.0318	0.0065
somitogenesis-switch [21]	821.18	4	10	4.6188	0.0690
smallest Hopf [71] (focus)	376.187	3	5	2.7065	0.0184
smallest Hopf [71] (Hopf)	468.307	3	5	3.3828	0.0181
smallest Hopf [71] (limit-cycle)	564.457	3	5	3.9284	0.0173
brusselator [39] (focus)	360.305	2	4	3.4655	0.0196
brusselator [39] (Hopf)	405.078	2	4	3.8119	0.0171
brusselator [39] (limit-cycle)	550.039	2	4	3.2390	0.0417
NF- κ B [4] (focus)	10986.9	11	25	44.8228	0.0276
NF- κ B [4] (Hopf)	9160.79	11	25	35.3062	0.0390
NF- κ B [4] (limit-cycle)	7661.71	11	25	27.1758	0.0264

Table 1: Computational time of SSA and pcLNA for different systems. The median CPU times for the SSA and pcLNA simulations with parameter values given in the SI Sections S4.1-S4.6 are displayed along with number of populations (n), reaction channels (r), and average number of reaction occurrences in thousands (N_r , see 6).

7 Discussion

The results in this paper demonstrate the capability of the modified LNA method to effectively capture non-linear dynamics over long time intervals. The modification introduced is justified by a novel reformulation of the LNA in coordinates that separate persistent non-linear dynamics from transient dynamics. The accuracy of the approximation combined with the analytical tractability of the LNA method, and speed of computation establishes a robust framework for investigating population dynamics, and fitting these models to data. It overcomes key limitations of existing methods and opens new avenues for advancing the stochastic modeling of dynamical systems.

We showcase the the versatility of our methodology across a range of systems exhibiting two fundamental forms of non-linear behavior—oscillations and bistability—which are common in biology and other scientific domains. Beyond these cases, our approach, grounded in centre manifold theory from dynamical systems, is applicable to a much broader class of reaction networks. Specifically, for any parameter-dependent network whose RRE solution features a non-hyperbolic equilibrium—a scenario frequently encountered in practice—the pcLNA algorithm enables fast and accurate simulation of long-term stochastic trajectories, even in large and complex systems.

Such stochastic simulations are essential for applications including *in silico* experimentation, and sensitivity analysis [32, 25, 67, 53, 41, 58, 8, 49], and statistical inference using Approximate Bayesian Computation methods [63, 44, 60, 65]. Moreover, this work lays the groundwork for future methods that leverage the long-term accuracy and analytical strengths of pcLNA—enabling, for instance, the exact computation of likelihood functions for time-series data, as well as key quantities like the Fisher Information, which are critical for assessing system sensitivity and robustness to parameter variation.

References

- [1] D.F. Anderson and T.G. Kurtz. *Continuous Time Markov Chain Models for Chemical Reaction Networks*, pages 3–42. Springer New York, 2011.
- [2] David Angeli, James E. Ferrell, and Eduardo D. Sontag. Detection of multistability, bifurcations, and hysteresis in a large class of biological positive-feedback systems. *Proceedings of the National Academy of Sciences*, 101:1822–1827, 2 2004.
- [3] Sol M. Fernández Arancibia, Hernán E. Grecco, and Luis G. Morelli. Effective description of bistability and irreversibility in apoptosis. *Phys. Rev. E*, 104:064410, Dec 2021.
- [4] L. Ashall, C.A. Horton, D.E. Nelson, P. Paszek, C.V. Harper, K. Sillitoe, S. Ryan, D.G. Spiller, J.F. Unitt, D.S. Broomhead, D.B. Kell, D.A. Rand, V. Sée, and M.R.H. White. Pulsatile stimulation determines timing and specificity of nf- κ b-dependent transcription. *Science (American Association for the Advancement of Science)*, 324(5924):242–246, 2009.
- [5] R.P. Boland, T. Galla, and A.J. McKane. How limit cycles and quasi-cycles are related in systems with intrinsic noise. *Journal of Statistical Mechanics: Theory and Experiment*, 2008, 9 2008.
- [6] Alexander Cao, Benjamin Lindner, and Peter J. Thomas. A partial differential equation for the mean–return-time phase of planar stochastic oscillators. *SIAM journal on applied mathematics*, 80(1):422–447, 2020.
- [7] Zhixing Cao and Ramon Grima. Linear mapping approximation of gene regulatory networks with stochastic dynamics. *Nature Communications*, 9:3305, 8 2018.
- [8] Harsh Chhajer and Rahul Roy. Rationalised experiment design for parameter estimation with sensitivity clustering. *Scientific Reports*, 14:25864, 10 2024.
- [9] Francis Corson and Eric Dean Siggia. Geometry, epistasis, and developmental patterning. *Proceedings of the National Academy of Sciences*, 109:5568–5575, 4 2012.
- [10] Mirela Domijan, Paul E. Brown, Boris V. Shulgin, and David A. Rand. Pettsy: a computational tool for perturbation analysis of complex systems biology models. *BMC Bioinformatics*, 17:124, 3 2016.
- [11] Maximilian Engel and Christian Kuehn. A random dynamical systems perspective on isochronicity for stochastic oscillations. *Communications in Mathematical Physics*, 386(3):1603–1641, 2021.
- [12] Bärbel Finkenstädt, Dan J. Woodcock, Michal Komorowski, Claire V. Harper, Julian R. E. Davis, Mike R. H. White, David a. Rand, Barbel Finkenstadt, Dan J. Woodcock, Michal Komorowski, Claire V. Harper, Julian R. E. Davis, Mike R. H. White, and David a. Rand. Quantifying intrinsic and extrinsic noise in gene transcription using the linear noise approximation: An application to single cell data. *The Annals of Applied Statistics*, 7:1960–1982, 12 2013.
- [13] Sorana Froda and Séverien Nkurunziza. Prediction of predator–prey populations modelled by perturbed odes. *Journal of Mathematical Biology*, 54(3):407–451, 2007.
- [14] Timothy S. Gardner, Charles R. Cantor, and James J. Collins. Construction of a genetic toggle switch in escherichia coli. *Nature*, 403:339–342, 1 2000.

- [15] D.T. Gillespie. A general method for numerically simulating the stochastic time evolution of coupled chemical reactions. *Journal of Computational Physics*, 22(4):403–434, 1976.
- [16] D.T. Gillespie. Exact stochastic simulation of coupled chemical reactions. *The Journal of Physical Chemistry*, 81(25):2340–2361, 1977.
- [17] D.T. Gillespie. A rigorous derivation of the chemical master equation. *Physica A*, 188(1):404–425, 1992.
- [18] D.T. Gillespie. The chemical Langevin equation. *The Journal of Chemical Physics*, 113(1):297–306, 07 2000.
- [19] D.T. Gillespie. Approximate accelerated stochastic simulation of chemically reacting systems. *The Journal of Chemical Physics*, 115(4):1716–1733, 07 2001.
- [20] D.T. Gillespie and L.R. Petzold. Improved leap-size selection for accelerated stochastic simulation. *The Journal of Chemical Physics*, 119(16):8229–8234, 10 2003.
- [21] Albert Goldbeter, Didier Gonze, and Olivier Pourquié. Sharp developmental thresholds defined through bistability by antagonistic gradients of retinoic acid and fgf signaling. *Developmental Dynamics*, 236:1495–1508, 6 2007.
- [22] Andrew Golightly, Laura E. Wadkin, Sam A. Whitaker, Andrew W. Baggaley, Nick G. Parker, and Theodore Kypraios. Accelerating bayesian inference for stochastic epidemic models using incidence data. *Statistics and Computing*, 33:134, 12 2023.
- [23] Didier Gonze, José Halloy, Jean-Christophe Leloup, and Albert Goldbeter. Stochastic models for circadian rhythms: effect of molecular noise on periodic and chaotic behaviour. *Comptes Rendus Biologies*, 326(2):189 – 203, 2003.
- [24] Theodore W. Grunberg and Domitilla Del Vecchio. A stein’s method approach to the linear noise approximation for stationary distributions of chemical reaction networks, 2024.
- [25] Ankit Gupta and Mustafa Khammash. An efficient and unbiased method for sensitivity analysis of stochastic reaction networks. *Journal of the Royal Society Interface*, 11:20140979–20140979, 2014.
- [26] A.V. Hill. The possible effects of the aggregation of the molecules of hæmoglobin on its dissociation curves. *The Journal of Physiology*, 40:i–vii, January 1910.
- [27] The MathWorks Inc. Matlab version: 9.13.0 (r2022b), 2022.
- [28] N. Ishii, K. Nakahigashi, T. Baba, M. Robert, T. Soga, A. Kanai, T. Hirasawa, M. Naba, K. Hirai, A. Hoque, P.Y. Ho, Y. Kakazu, K. Sugawara, S. Igarashi, S. Harada, T. Masuda, N. Sugiyama, T. Togashi, M. Hasegawa, Y. Takai, K. Yugi, K. Arakawa, N. Iwata, Y. Toya, Y. Nakayama, T. Nishioka, K. Shimizu, H. Mori, and M. Tomita. Multiple high-throughput analyses monitor the response of e. coli to perturbations. *Science (American Association for the Advancement of Science)*, 316(5824):593–597, 2007.
- [29] Y. Ito and K. Uchida. Formulas for intrinsic noise evaluation in oscillatory genetic networks. *Journal of Theoretical Biology*, 267:223–234, 11 2010.
- [30] Chen Jia and Ramon Grima. Holimap: an accurate and efficient method for solving stochastic gene network dynamics. *Nature Communications*, 15:6557, 8 2024.

- [31] K.A. Johnson and R.S. Goody. The original michaelis constant: Translation of the 1913 michaelis–menten paper. *Biochemistry (Easton)*, 50(39):8264–8269, 2011.
- [32] Michal Komorowski, Maria J Costa, David a Rand, and Michael P H Stumpf. Sensitivity, robustness, and identifiability in stochastic chemical kinetics models. *Proceedings of the National Academy of Sciences of the United States of America*, 108:8645–8650, 5 2011.
- [33] Michal Komorowski, Barbel Finkenstadt, Claire V Harper, David a Rand, Bärbel Finkenstädt, Claire V Harper, David a Rand, Barbel Finkenstadt, Claire V Harper, and David a Rand. Bayesian inference of biochemical kinetic parameters using the linear noise approximation. *BMC Bioinformatics*, 10:343, 10 2009.
- [34] T.G. Kurtz. Limit theorems for sequences of jump markov processes approximating ordinary differential processes. *Journal of Applied Probability*, 8(2):344–356, 1971.
- [35] T.G. Kurtz, Society for Industrial, and Applied Mathematics. *Approximation of Population Processes*. Number nos. 36-40 in Approximation of Population Processes. Society for Industrial and Applied Mathematics, 1981.
- [36] Thomas G. Kurtz. Strong approximation theorems for density dependent markov chains. *Stochastic Processes and their Applications*, 6(3):223–240, 1978.
- [37] Y. Kuznetsov. *Elements of Applied Bifurcation Theory, 3rd Edic.* Society for Industrial and Applied Mathematics, 2011.
- [38] J. F. Le Gall. *Brownian motion, martingales, and stochastic calculus*. Graduate texts in mathematics, 274. Springer, Switzerland, 2016.
- [39] R. Lefever and G. Nicolis. Chemical instabilities and sustained oscillations. *Journal of Theoretical Biology*, 30(2):267–284, 1971.
- [40] Ioannis Lestas, Johan Paulsson, Nicholas E. Ross, and Glenn Vinnicombe. Noise in gene regulatory networks. *IEEE Transactions on Automatic Control*, 53:189–200, 1 2008.
- [41] Juliane Liepe, Paul Kirk, Sarah Filippi, Tina Toni, Chris P Barnes, and Michael P H Stumpf. A framework for parameter estimation and model selection from experimental data in systems biology using approximate bayesian computation. *Nature Protocols*, 9:439–456, 2 2014.
- [42] S. Mangan and U. Alon. Structure and function of the feed-forward loop network motif. *Proceedings of the National Academy of Sciences*, 100:11980–11985, 10 2003.
- [43] Elli Marinopoulou, Veronica Biga, Nitin Sabherwal, Anzy Miller, Jayni Desai, Antony D. Adamson, and Nancy Papalopulu. Hes1 protein oscillations are necessary for neural stem cells to exit from quiescence. *iScience*, 24:103198, 10 2021.
- [44] Paul Marjoram, John Molitor, Vincent Plagnol, and Simon Tavaré. Markov chain monte carlo without likelihoods. *Proceedings of the National Academy of Sciences*, 100:15324–15328, 12 2003.
- [45] Naoki Masuda and Christian L. Vestergaard. *Gillespie Algorithms for Stochastic Multiagent Dynamics in Populations and Networks*. Cambridge University Press, 1 2023.
- [46] G. Minas and D.A. Rand. Long-time analytic approximation of large stochastic oscillators: Simulation, analysis and inference. *PLoS Computational Biology*, 13, 7 2017.

- [47] G. Minas and D.A. Rand. Parameter sensitivity analysis for biochemical reaction networks. *Mathematical biosciences and engineering : MBE*, 16(5):3965–3987, 2019.
- [48] G. Minas, D.J. Woodcock, L. Ashall, C. Harper, M.R.H. White, and D.A. Rand. Multiplexing information flow through dynamic signalling systems. *PLoS computational biology*, 16(8):e1008076–e1008076, 2020.
- [49] Giorgos Minas and David A Rand. Parameter sensitivity analysis for biochemical reaction networks. *Mathematical Biosciences and Engineering*, 16:3965–3987, 4 2019.
- [50] Bela Novak and John J. Tyson. Numerical analysis of a comprehensive model of m-phase control in xenopus oocyte extracts and intact embryos. *Journal of Cell Science*, 106:1153–1168, 12 1993.
- [51] J. Palis and F. Takens. Stability of parametrized families of gradient vector fields. *Annals of Mathematics*, 118(3):383–421, 1983.
- [52] Joseph R. Pomerening, Sun Young Kim, and James E. Ferrell. Systems-level dissection of the cell-cycle oscillator: Bypassing positive feedback produces damped oscillations. *Cell*, 122:565–578, 8 2005.
- [53] Tom Rainforth, Adam Foster, Desi R. Ivanova, and Freddie Bickford Smith. Modern bayesian experimental design. *Statistical Science*, 39, 2 2024.
- [54] Nitzan Rosenfeld, Michael B Elowitz, and Uri Alon. Negative autoregulation speeds the response times of transcription networks. *Journal of Molecular Biology*, 323:785–793, 11 2002.
- [55] David Schnoerr, Guido Sanguinetti, and Ramon Grima. Approximation and inference methods for stochastic biochemical kinetics - a tutorial review. *Journal of Physics A: Mathematical and Theoretical*, 50, 8 2016.
- [56] J. T. C Schwabedal and A Pikovsky. Effective phase description of noise-perturbed and noise-induced oscillations: The dynamics of nonlinear stochastic systems. *The European physical journal. ST, Special topics*, 187:63–76, 2010.
- [57] M. Scott, B. Ingalls, and M. Kærn. Estimations of intrinsic and extrinsic noise in models of nonlinear genetic networks. *Chaos*, 16, 2006.
- [58] Ali Shahmohammadi and Kimberley B. McAuley. Using prior parameter knowledge in model-based design of experiments for pharmaceutical production. *AIChE Journal*, 66, 11 2020.
- [59] A. N. Shoshitaishvili. Bifurcations of topological type at singular points of parametrized vector fields. *Functional analysis and its applications*, 6(2):169–170, 1972.
- [60] S. A. Sisson, Y. Fan, and Mark M. Tanaka. Sequential monte carlo without likelihoods. *Proceedings of the National Academy of Sciences*, 104:1760–1765, 2 2007.
- [61] B. Swallow, D.A. Rand, and G. Minas. Bayesian inference for stochastic oscillatory systems using the phase-corrected linear noise approximation. *Bayesian Analysis*, pages 1 – 30, 2024.
- [62] Floris Takens. Partially hyperbolic fixed points. *Topology (Oxford)*, 10(2):133–147, 1971.
- [63] Simon Tavaré, David J Balding, R C Griffiths, and Peter Donnelly. Inferring coalescence times from dna sequence data. *Genetics*, 145:505–518, 2 1997.

- [64] P. Thomas, H. Matuschek, and R. Grima. How reliable is the linear noise approximation of gene regulatory networks? *BMC Genomics*, 14, 2013.
- [65] Tina Toni, David Welch, Natalja Strelkowa, Andreas Ipsen, and Michael P.H Stumpf. Approximate bayesian computation scheme for parameter inference and model selection in dynamical systems. *Journal of The Royal Society Interface*, 6:187–202, 2 2009.
- [66] N.G. van Kampen. *Stochastic Processes in Physics and Chemistry*. Elsevier Science Publishers, Amsterdam, 1992.
- [67] Joep Vanlier, Christian A Tiemann, Peter AJ Hilbers, and Natal AW van Riel. Optimal experiment design for model selection in biochemical networks. *BMC Systems Biology*, 8:20, 2014.
- [68] P. Waage and C.M. Gulberg. Studies concerning affinity. *Journal of chemical education*, 63(12):1044–, 1986.
- [69] E.W.J. Wallace, D.T. Gillespie, K.R. Sanft, and L.R. Petzold. Linear noise approximation is valid over limited times for any chemical system that is sufficiently large. *IET Systems Biology*, 6:102–115, 8 2012.
- [70] Joshua S. Weitz, Sang Woo Park, Ceyhun Eksin, and Jonathan Dushoff. Awareness-driven behavior changes can shift the shape of epidemics away from peaks and toward plateaus, shoulders, and oscillations. *Proceedings of the National Academy of Sciences*, 117:32764–32771, 12 2020.
- [71] T. Wilhelm and R. Heinrich. Smallest Chemical-Reaction System With Hopf-Bifurcation. *J Math Chem*, 17:1–14, 1995.
- [72] Darren James Wilkinson. *Stochastic modelling for systems biology*, 2012.

Supporting Information (SI)

The SI contains further mathematical details and numerical investigations referenced in the main paper. We used PeTTTSy [10] implemented in the MATLAB [27] environment and available at <https://wrap.warwick.ac.uk/id/eprint/77654/> to produce all results.

S1 The stochastic simulation algorithm (SSA)

Consider paths of $\{\mathbf{Y}(t) \mid t \geq 0\}$ whose time-evolution is given by the random time change representation (RTC),

$$\mathbf{Y}(t) = \mathbf{Y}(0) + \sum_{j=1}^r \nu_j N_j \left(\int_0^t \pi_j(\mathbf{Y}(s)) ds \right), \quad (32)$$

where, for $j \in \{1, \dots, r\}$, N_j are independent, unit Poisson processes corresponding to reaction R_j . To simulate such paths, the stochastic simulation algorithm (SSA) generates the next reaction at any given state. That is, if $\hat{\tau} > 0$ and $k \in \{1, 2, \dots, r\}$ correspond to the time to the next reaction and the index of the next reaction, respectively, it can be shown that, given the current state at time $t \geq 0$, $\mathbf{Y}(t) = \mathbf{y}$, the joint probability density function $p(\hat{\tau}, k \mid \mathbf{y}, t)$ of $\hat{\tau}$ and k are

$$p(\hat{\tau}, k \mid \mathbf{y}, t) = \pi_k(\mathbf{y}) \exp \left(- \sum_{j=1}^r \pi_j(\mathbf{y}) \tau \right). \quad (33)$$

where π_k the propensity function of reaction k . Informally, $p(\hat{\tau}, k \mid \mathbf{y}, t) d\tau$ represents the probability that, given that $\mathbf{Y}(t) = \mathbf{y}$, the next reaction in the system will occur at in the infinitesimal time interval $[t + \hat{\tau}, t + \hat{\tau} + d\hat{\tau})$ and will be a R_k reaction. Equation (33) implies that $\hat{\tau}$ is an exponential random variable with mean $1 / \sum_{j=1}^r \pi_j(\mathbf{y})$ and k is a statistically independent to τ integer random variable with point probabilities $\pi_k(\mathbf{y}) / \sum_{j=1}^r \pi_j(\mathbf{y})$. Hence we can sample such random variables exactly using the following; generate two random numbers, r_1 and r_2 , from the uniform distribution in the unit interval and take,

$$\hat{\tau} = - \frac{\log(r_1)}{\sum_{j=1}^r \pi_j(\mathbf{y})}, \quad (34)$$

and k to be the smallest integer with $k \leq r$ such that,

$$\sum_{j=1}^k \pi_j(\mathbf{y}) > r_2 \sum_{j=1}^r \pi_j(\mathbf{y}). \quad (35)$$

Using the sampling procedure given by (34) and (35), we are able to construct the SSA for paths of $\{\mathbf{Y}(t) \mid t \geq 0\}$ which evolve exactly according to (4). This is given in Algorithm 4.

Here the output sequence (t_j, \mathbf{y}_j) , $j = 1, 2, \dots$, fully describes the evolution of a stochastic trajectory $\{\mathbf{Y}(t) : 0 \leq t \leq T\}$. Note that $\mathbf{Y}(t) = \mathbf{y}(t_j)$ for $t_j \leq t < t_{j+1}$. These paths are exact consequences of the chemical physics of stochastic reaction networks and hence capture the true dynamics of the network. For further details see [15, 16]. Consequently, one can compare distributions of states simulated by a model to that by the SSA in order to test the statistical accuracy of the model.

Algorithm 4 Stochastic Simulation Algorithm (SSA)

Inputs: Initial conditions: $t_0 = 0$, $\mathbf{Y}(0) = \mathbf{y}_0$, $i = 0$. Parameter $T > 0$.

Steps: While $t < T$

1. generate two random numbers, r_1 and r_2 , from the uniform distribution on the unit interval;
2. sample $\hat{\tau}$ according to (34) and k according to (35);
3. update $t \leftarrow t + \hat{\tau}$ and $\mathbf{y} \leftarrow \mathbf{y} + \boldsymbol{\nu}_k$;
4. update $i \leftarrow i + 1$ and store t in t_i and \mathbf{y} in \mathbf{y}_i .

Outputs: (t_j, \mathbf{y}_j) , $j = 1, \dots, i$

Algorithm 5 SSA with thinning

Inputs: Initial conditions: $t_0 = 0$, $\mathbf{Y}(0) = \mathbf{y}_0$, $i = 0$, $m = 1$. Parameter $T > 0$, $\delta t > 0$, M positive integer.

Steps: While $t < T$ and $m \leq M$

1. generate two random numbers, r_1 and r_2 , from the uniform distribution on the unit interval;
2. sample $\hat{\tau}$ according to (34) and k according to (35);
3. update $t \leftarrow t + \hat{\tau}$ and $\mathbf{y} \leftarrow \mathbf{y} + \boldsymbol{\nu}_k$;
4. update $i \leftarrow i + 1$ and
 - if $t \in (m\delta t, (m+1)\delta t)$, then store t in t_m and \mathbf{y} in \mathbf{y}_m , and update $m \leftarrow m + 1$,
 - if $t > (m+1)\delta t$, end procedure with message “increase δt and run again.”.

Outputs: (t_j, \mathbf{y}_j) , $j = 1, \dots, m$

When performing the SSA simulations, we used the so-called *thinning* method to reduce the computational memory used. That is, we used the Algorithm 5. This records the SSA generated states at the first reaction times after times $m\delta t$, $m = 0, 1, 2, \dots, M$, for some large M and fairly small δt . Furthermore, when we wish to compare SSA with pcLNA at specific times we use a smoothing spline interpolation to get the state of SSA (and similarly pcLNA) at specific time, say $t \in [(m-1)\delta t, m\delta t]$.

S2 The derivation of the Linear Noise Approximation (LNA)

The following is a heuristic derivation of the LNA equations, similar to this provided in [1]. For a formal derivation see [36]. To simplify notation, in this section we use the notation $x_t = x(t)$, for all states considered (i.e. \mathbf{x} , $\boldsymbol{\xi}$, \mathbf{X}). The LNA ansatz,

$$\mathbf{X}_t = \mathbf{x}_t + \Omega^{-1/2} \boldsymbol{\xi}_t,$$

implies that

$$\boldsymbol{\xi}_t = \sqrt{\Omega}(\mathbf{X}_t - \mathbf{x}_t)$$

and thus

$$\boldsymbol{\xi}_{t+dt} - \boldsymbol{\xi}_t = \sqrt{\Omega}((\mathbf{X}_{t+dt} - \mathbf{X}_t) - (\mathbf{x}_{t+dt} - \mathbf{x}_t)).$$

Using the form of RTC for \mathbf{X} and the RRE, we get that

$$\boldsymbol{\xi}_{t+dt} - \boldsymbol{\xi}_t = \sqrt{\Omega} \left(\sum_{j=1}^r \boldsymbol{\nu}_j \{ \Omega^{-1} N_j (\Omega \rho_j(\mathbf{X}_t) dt) - \rho_j(\mathbf{x}_t) dt \} \right).$$

We next insert in the above sum the zero terms $0 = \rho_j(\mathbf{X}_t) dt - \rho_j(\mathbf{x}_t) dt$, where $\rho_j(\mathbf{X}_t) dt$ the mean of $\Omega^{-1} N_j (\Omega \rho_j(\mathbf{X}_t) dt)$, to get

$$\boldsymbol{\xi}_{t+dt} - \boldsymbol{\xi}_t = \sqrt{\Omega} \left(\sum_{j=1}^r \boldsymbol{\nu}_j \{ \Omega^{-1} N_j (\Omega \rho_j(\mathbf{X}_t) dt) - \rho_j(\mathbf{X}_t) dt + (\rho_j(\mathbf{X}_t) - \rho_j(\mathbf{x}_t)) dt \} \right).$$

Then, by the Central Limit Theorem, as $\Omega \rightarrow \infty$,

$$Z = \frac{\Omega^{-1} N_j (\Omega \rho_j(\mathbf{X}_t) dt) - \rho_j(\mathbf{X}_t) dt}{\sqrt{\Omega^{-1} \rho_j(\mathbf{X}_t) dt}} \sim N(0, 1)$$

where $N(0, 1)$ is the standard normal distribution. Then for sufficiently large Ω ,

$$\sqrt{\Omega} (\Omega^{-1} N_j (\Omega \rho_j(\mathbf{X}_t) dt) - \rho_j(\mathbf{X}_t) dt) \approx Z \sqrt{\rho_j(\mathbf{x}_t) dt}. \quad (36)$$

Furthermore, by applying a Taylor expansion of $\rho_j(\mathbf{X}_t)$ about \mathbf{x}_t , we get

$$\sqrt{\Omega} (\rho_j(\mathbf{X}_t) - \rho_j(\mathbf{x}_t)) = \boldsymbol{\xi}(t)^\top \nabla_{\mathbf{x}} \rho_j(\mathbf{x}_t) + O(\Omega^{-1/2}), \quad (37)$$

where $\nabla_{\mathbf{x}}^\top = (\partial/\partial x_1, \dots, \partial/\partial x_n)$. Hence, for sufficiently large Ω ,

$$\boldsymbol{\xi}_{t+dt} - \boldsymbol{\xi}_t \approx \sum_j \lambda_j \boldsymbol{\xi}(t)^\top \nabla_{\mathbf{x}} \rho_j(\mathbf{x}_t) dt + \sum_j Z_j \lambda_j \sqrt{\rho_j(\mathbf{x}_t) dt}$$

where Z_j are independent random variables following the standard normal distribution. Writing the above equation in matrix form, we get

$$d\boldsymbol{\xi}_t = \mathbf{J}_t \boldsymbol{\xi}_t dt + \mathbf{E}_t d\mathbf{B}_t, \quad (38)$$

where $\mathbf{J}_t = \mathbf{J}(\mathbf{x}_t)$ is the Jacobian matrix of the RRE (6), and

$$\mathbf{E}_t = \mathbf{E}(\mathbf{x}_t) = \mathbf{S} \text{diag} \left(\sqrt{\rho_1(\mathbf{x}_t)}, \dots, \sqrt{\rho_r(\mathbf{x}_t)} \right)$$

the product of the stoichiometry matrix $\mathbf{S} = [\boldsymbol{\nu}_1 \cdots \boldsymbol{\nu}_r]$, and the square root of the diagonal matrix, with main diagonal entries $(\rho_1(\mathbf{x}), \dots, \rho_r(\mathbf{x}))$, while \mathbf{B}_t an n -dimensional Wiener process.

S3 Centre manifold theory

For a more detailed introduction to centre manifold theory see [37].

Different dynamical systems can be grouped together based on the qualitative similarity of their behavior near their equilibrium points.

Definition 1 (Topological equivalence). *Consider two ODE systems as in 6 with velocities \mathbf{F} and \mathbf{F}' on \mathbb{R}^n and \mathbb{R}^m respectively. Suppose they each have an equilibrium point \mathbf{x}_0 and \mathbf{x}'_0 , respectively. Then, near their equilibrium, the two dynamical systems are locally topologically equivalent if there exists a homeomorphism $\mathbf{h} : \mathbb{R}^n \rightarrow \mathbb{R}^m$ that is*

- (i) *defined in a neighbourhood $A \subset \mathbb{R}^n$ of \mathbf{x}_0 ;*
- (ii) *satisfies $\mathbf{x}'_0 = \mathbf{h}(\mathbf{x}_0)$;*
- (iii) *maps paths of the system with velocity \mathbf{F} in A onto paths of the system with velocity \mathbf{F}' in $\mathbf{h}(A) \subset \mathbb{R}^m$, preserving the direction of time.*

Intuitively, this means the paths of one dynamical system near its equilibrium can be continuously deformed onto paths of the other dynamical system near its equilibrium, and hence both systems exhibit qualitatively similar behavior near their equilibria.

Extended system and non-hyperbolic equilibrium Consider the deterministic evolution solving the reaction rate equation (6) when one parameter $\alpha \in \mathbb{R}$ is free to vary. Assume there exists $\alpha_p \in \mathbb{R}$ such that

$$\mathbf{F}(\mathbf{x}_{\alpha_p}, \alpha_p) = \mathbf{0} \quad \text{and} \quad n_0 > 0, \quad (39)$$

where n_0, n_+, n_- denote the number of eigenvalues of the Jacobian matrix $\mathbf{J}(\mathbf{x}_{\alpha_p}, \alpha_p)$ with zero, positive and negative real part, respectively.

Introduce the extended autonomous system

$$\begin{cases} \dot{\mathbf{x}} = \mathbf{F}(\mathbf{x}, \alpha), \\ \dot{\alpha} = 0, \end{cases} \quad (40)$$

whose Jacobian at $(\mathbf{x}, \alpha) = (\mathbf{x}_{\alpha_p}, \alpha_p)$ is

$$\mathcal{A} := \begin{pmatrix} \mathbf{J}(\mathbf{x}_{\alpha_p}, \alpha_p) & \partial_\alpha \mathbf{F}(\mathbf{x}_{\alpha_p}, \alpha_p) \\ \mathbf{0} & 0 \end{pmatrix}. \quad (41)$$

This matrix has $n_0 + 1$ eigenvalues with zero real part and $n - n_0$ eigenvalues with nonzero real part.

Theorem 1 (Center Manifold Theorem). *Let E^c denote the eigenspace of \mathcal{A} corresponding to the $n_0 + 1$ eigenvalues with zero real part. Then there exists a smooth $(n_0 + 1)$ -dimensional invariant manifold \mathcal{W}^c , defined locally near $(\mathbf{x}_{\alpha_p}, \alpha_p)$ and tangent to E^c at that point.*

Since $\dot{\alpha} = 0$, the hyperplanes

$$\Pi_{\alpha'} := \{(\mathbf{x}, \alpha) \mid \alpha = \alpha'\}, \quad \alpha' \in \mathbb{R},$$

are invariant under (40). Consequently, for each α near α_p , the center manifold is foliated by n_0 -dimensional invariant manifolds

$$\mathcal{W}_\alpha^c := \mathcal{W}^c \cap \Pi_\alpha,$$

which we call the centre manifolds. Moreover, for each such α , there exists a neighbourhood $\Delta(\mathbf{x}_{\alpha_p})$ such that any trajectory of (40) starting in $\Delta(\mathbf{x}_{\alpha_p})$ either converges to \mathcal{W}_α^c or leaves $\Delta(\mathbf{x}_{\alpha_p})$ exponentially fast as $t \rightarrow \infty$.

Takens normal form for the extended system Let $\lambda_1, \dots, \lambda_{n_{cu}}$, where $n_{cu} = n_0 + n_- + 1$, denote the eigenvalues of \mathcal{A} with zero or negative real part including the zero eigenvalue associated with $\dot{\alpha} = 0$. For each integer $k \geq 1$, we say that (40) satisfies the *k-Sternberg nonresonance condition* (see [62, Definition 2 and Section 4]) if the following holds: for any choice of integers $c_1, \dots, c_{n_{cu}}$ satisfying

$$2 \leq \sum_{i=1}^{n_{cu}} c_i \leq \gamma(\mathcal{A}, k),$$

the sums,

$$\sum_{i=1}^{n_{cu}} c_i \lambda_i \neq 0, \quad -\lambda_j + \sum_{i=1}^{n_{cu}} c_i \lambda_i \neq 0 \quad \text{for all } j = 1, \dots, n_{cu}.$$

Here the integer $\gamma(\mathcal{A}, k)$ is defined as follows. Here we use the notation $\Re(\mu)$ to denote the real part of an eigenvalue μ . Let $\mu_1, \dots, \mu_{n_- + n_+}$ denote the eigenvalues of \mathcal{A} with non zero real part, ordered so that

$$\Re(\mu_1) \leq \dots \leq \Re(\mu_{n_-}) < 0 < \Re(\mu_{n_- + 1}) \leq \dots \leq \Re(\mu_{n_- + n_+}).$$

Define

$$\overline{M} := \max_{i > n_-} \Re(\mu_i), \quad \overline{m} := \min_{i > n_-} \Re(\mu_i), \quad \overline{N} := \max_{i \leq n_-} |\Re(\mu_i)|, \quad \overline{n} := \min_{i \leq n_-} |\Re(\mu_i)|.$$

Then $\beta(\mathcal{A}, k)$ is the smallest integer such that

$$\overline{N} + r \overline{M} - (r - \beta(\mathcal{A}, k)) \overline{n} < 0 \quad \text{for all integers } r \leq k,$$

and $\gamma(\mathcal{A}, k)$ is the smallest integer such that

$$\overline{M} + r \overline{N} - (r - \gamma(\mathcal{A}, k)) \overline{m} < 0 \quad \text{for all integers } r \leq \beta(\mathcal{A}, k).$$

The above conditions hold for almost all values of parameter α . In reaction networks, the free parameters α are typically reaction rate constants, for which the eigenvalues λ_i of the Jacobian depend smoothly. Resonance requires exact relations of the form $\sum_i c_i \lambda_i = 0$ for integers c_i , which occur only on sets of Lebesgue measure zero in parameter space and are destroyed by arbitrarily small parameter perturbations. Consequently, for analytical purposes the nonresonance conditions are satisfied almost surely, and for practical simulation purposes they can be enforced by arbitrarily small perturbations of the parameter α that do not affect the qualitative dynamics.

The following theorem requires these conditions to hold for all integers $k \geq 2$. It is therefore sufficient—and in practice straightforward—to verify that they hold for a given system for the cases $k = 1, 2$.

For the remainder of this section, assume that (40) satisfies the *k-Sternberg nonresonance condition* for some integer $k \geq 2$. Then the following theorem, first proved in [62, Section 4], holds. Below we use the notation C^m , $m \in \{1, 2, \dots\}$, to denote the set of functions that have a m -th derivative that is continuous in its domain.

Theorem 2 (Takens). *Suppose \mathbf{F} in (40) is C^∞ and the above *k-Sternberg nonresonance condition* holds for some $k \geq 2$. Then there exists a local C^k change of coordinates*

$$(\mathbf{x}, \alpha) \mapsto (\mathbf{u}, \mathbf{v}, \mathbf{w}, \alpha), \quad \mathbf{u} \in \mathbb{R}^{n_0}, \quad \mathbf{v} \in \mathbb{R}^{n_-}, \quad \mathbf{w} \in \mathbb{R}^{n_+},$$

defined near $(\mathbf{x}_{\alpha_p}, \alpha_p)$, such that the centre manifold \mathcal{W}_α^c in Theorem 1 is mapped precisely onto the linear subspace

$$\{(\mathbf{u}, \mathbf{v}, \mathbf{w}, \alpha) : \mathbf{v} = \mathbf{w} = 0\},$$

and the extended system (40) takes the standard form

$$\begin{cases} \dot{\mathbf{u}} = \mathbf{f}(\mathbf{u}, \alpha), \\ \dot{\mathbf{v}} = \mathbf{A}_s(\mathbf{u}, \alpha)\mathbf{v}, \\ \dot{\mathbf{w}} = \mathbf{A}_u(\mathbf{u}, \alpha)\mathbf{w}, \\ \dot{\alpha} = 0, \end{cases} \quad (42)$$

where $\mathbf{f}, \mathbf{A}_s, \mathbf{A}_u$ are C^k functions, all eigenvalues of the $n_- \times n_-$ matrix $\mathbf{A}_s(\mathbf{u}(t), \alpha)$ have negative real part, and all eigenvalues of the $n_+ \times n_+$ matrix $\mathbf{A}_u(\mathbf{u}(t), \alpha)$ have positive real part.

In particular, the reduced dynamics on \mathcal{W}_α^c is represented solely by the evolution of the centre coordinates \mathbf{u} , while the stable and unstable coordinates (\mathbf{v}, \mathbf{w}) evolve according to the linear equations determined by $\mathbf{A}_s(\mathbf{u}, \alpha)$ and $\mathbf{A}_u(\mathbf{u}, \alpha)$.

Relation to local topological equivalence From Theorem 2, there exist neighbourhoods

$$\mathcal{E} \subset \mathbb{R}^n \text{ of } \mathbf{x}_{\alpha_p}, \quad \mathcal{F} \subset \mathbb{R}^{n_0+n_-+n_+} \text{ of the origin,}$$

and an interval $\mathcal{I} \subset \mathbb{R}$ containing α_p , such that the coordinate transformation

$$(\mathbf{x}, \alpha) \mapsto (\mathbf{u}, \mathbf{v}, \mathbf{w}, \alpha)$$

is a C^k diffeomorphism from $\mathcal{E} \times \mathcal{I}$ onto $\mathcal{F} \times \mathcal{I}$.

For each fixed $\alpha \in \mathcal{I}$, restricting this transformation to the invariant hyperplane

$$\Pi_\alpha = \{(\mathbf{x}, \alpha) \in \mathbb{R}^{n+1}\}$$

in Theorem 1, defines a C^k diffeomorphism

$$\mathbf{h}_\alpha : \mathcal{E}_\alpha \longrightarrow \mathcal{F}_\alpha, \quad \mathbf{x} \mapsto (\mathbf{u}, \mathbf{v}, \mathbf{w}),$$

where

$$\mathcal{E}_\alpha := \mathcal{E} \cap \{\mathbf{x} : (\mathbf{x}, \alpha) \in \Pi_\alpha\}, \quad \text{and} \quad \mathcal{F}_\alpha := \mathbf{h}_\alpha(\mathcal{E}_\alpha).$$

Under this mapping, trajectories of the original system (6) in \mathcal{E}_α correspond to trajectories of the standard-form system (42) in \mathcal{F}_α with the same time orientation. Consequently, for each $\alpha \in \mathcal{I}$, the map \mathbf{h}_α realises the local topological equivalence of Definition 1 between the original system (6) in \mathcal{E}_α and the standard-form system (42) in \mathcal{F}_α .

Eigenspace projection approximation of the centre coordinates Although \mathbf{h}_α mapping the original coordinates \mathbf{x} to the centre–stable–unstable coordinates $(\mathbf{u}, \mathbf{v}, \mathbf{w})$ is in general nonlinear, its action on the centre coordinates admits a simple first-order approximation near the non-hyperbolic equilibrium \mathbf{x}_{α_p} . By construction, the centre manifold \mathcal{W}_α^c is tangent at \mathbf{x}_{α_p} to the eigenspace E^c associated with the eigenvalues of $\mathbf{J}(\mathbf{x}_{\alpha_p}, \alpha_p)$ having zero real part. Consequently, the differential $\nabla_{\mathbf{x}} \mathbf{h}_\alpha(\mathbf{x}_{\alpha_p})$ restricted to the centre coordinates coincides with the linear projection onto E^c .

Let $\mathbf{R}_c \in \mathbb{R}^{n \times n_0}$ denote a matrix whose columns form a basis of this eigenspace, and define the associated projection $\mathbf{P}_c := \mathbf{R}_c^{-1}$ onto the centre coordinates. Then, for any state \mathbf{X} sufficiently close to \mathbf{x}_{α_p} , the centre component \mathbf{U} of $\mathbf{h}_\alpha(\mathbf{X})$ satisfies

$$\mathbf{U} = \mathbf{P}_c(\mathbf{X} - \mathbf{x}_{\alpha_p}) + O(\|\mathbf{X} - \mathbf{x}_{\alpha_p}\|^2). \quad (43)$$

This approximation shows that, to leading order, the nonlinear centre coordinates are obtained simply by projecting deviations from the equilibrium onto E^c .

Application of Itô's Lemma to the image of the LNA under the local homeomorphism

To simplify notation as before, in this section we use the notation $x_t = x(t)$, for all states considered (i.e. \mathbf{x} , $\boldsymbol{\xi}$, \mathbf{X}). Under the non-resonance conditions on the eigenvalues of $\mathbf{J}(\mathbf{x}_{\alpha_p}, \alpha_p)$ required for Theorem 2, the mapping $\mathbf{h}_\alpha : \mathcal{E}_\alpha \rightarrow \mathcal{F}_\alpha$ is C^k for some $k \geq 2$. Given that $\mathbf{X}_0 = \mathbf{x}_0 + \Omega^{-1/2}\boldsymbol{\xi}_0 \in \mathcal{E}_\alpha$, this level of regularity is sufficient to apply Itô's Lemma (see [38, Theorem 5.10]) to the image of the continuous semimartingale $\mathbf{X}_t = \mathbf{x}_t + \Omega^{-1/2}\boldsymbol{\xi}_t$ under \mathbf{h}_α and obtain an SDE representation of its evolution for times $t \in [0, \tau)$ where,

$$\tau := \inf\{t \geq 0 : \mathbf{X}_t = \mathbf{x}_t + \Omega^{-1/2}\boldsymbol{\xi}_t \notin \mathcal{E}_\alpha\}.$$

To this end,

$$\begin{aligned} d\mathbf{h}_\alpha(\mathbf{X}_t) &= \nabla_{\mathbf{x}}\mathbf{h}_\alpha(\mathbf{X}_t) d\mathbf{X}_t + \frac{1}{2\Omega} \text{Tr}(\mathbf{E}_t^\top \nabla_{\mathbf{x}}^2 \mathbf{h}_\alpha(\mathbf{X}_t) \mathbf{E}_t) dt \\ &= \nabla_{\mathbf{x}}\mathbf{h}_\alpha(\mathbf{X}_t) \left(\mathbf{F}(\mathbf{x}_t, \alpha) + \frac{1}{\sqrt{\Omega}} \mathbf{J}_t \boldsymbol{\xi}_t \right) dt \\ &\quad + \frac{1}{\sqrt{\Omega}} \nabla_{\mathbf{x}}\mathbf{h}_\alpha(\mathbf{X}_t) \mathbf{E}_t d\mathbf{B}_t + \frac{1}{2\Omega} \text{Tr}(\mathbf{E}_t^\top \nabla_{\mathbf{x}}^2 \mathbf{h}_\alpha(\mathbf{X}_t) \mathbf{E}_t) dt. \end{aligned} \quad (44)$$

Taylor expanding $\nabla_{\mathbf{x}}\mathbf{h}_\alpha(\mathbf{X}_t) = \nabla_{\mathbf{x}}\mathbf{h}_\alpha(\mathbf{x}_t + \Omega^{-1/2}\boldsymbol{\xi}_t)$ about \mathbf{x}_t gives

$$\nabla_{\mathbf{x}}\mathbf{h}_\alpha(\mathbf{X}_t) = \nabla_{\mathbf{x}}\mathbf{h}_\alpha(\mathbf{x}_t) + \frac{1}{\sqrt{\Omega}} \boldsymbol{\xi}_t^\top \nabla_{\mathbf{x}}^2 \mathbf{h}_\alpha(\mathbf{x}_t) + O(\Omega^{-1}),$$

and so (44) becomes,

$$\begin{aligned} d\mathbf{h}_\alpha(\mathbf{X}_t) &= \left(\nabla_{\mathbf{x}}\mathbf{h}_\alpha(\mathbf{x}_t) \mathbf{F}(\mathbf{x}_t, \alpha) + \frac{1}{\sqrt{\Omega}} \boldsymbol{\xi}_t^\top \nabla_{\mathbf{x}}^2 \mathbf{h}_\alpha(\mathbf{x}_t) \mathbf{F}(\mathbf{x}_t, \alpha) \right. \\ &\quad \left. + \frac{1}{\sqrt{\Omega}} \nabla_{\mathbf{x}}\mathbf{h}_\alpha(\mathbf{x}_t) \mathbf{J}_t \boldsymbol{\xi}_t \right) dt + \frac{1}{\sqrt{\Omega}} \nabla_{\mathbf{x}}\mathbf{h}_\alpha(\mathbf{x}_t) \mathbf{E}_t d\mathbf{B}_t + O(\Omega^{-1}). \end{aligned} \quad (45)$$

By Theorem 2, $(\mathbf{u}_t, \mathbf{v}_t, \mathbf{w}_t)^\top := \mathbf{h}_\alpha(\mathbf{x}_t)$ evolves according to (42) and hence

$$\frac{d}{dt}(\mathbf{u}_t, \mathbf{v}_t, \mathbf{w}_t) = \frac{d}{dt}\mathbf{h}_\alpha(\mathbf{x}_t) = \nabla_{\mathbf{x}}\mathbf{h}_\alpha(\mathbf{x}_t) \frac{d}{dt}\mathbf{x}_t = \nabla_{\mathbf{x}}\mathbf{h}_\alpha(\mathbf{x}_t) \mathbf{F}(\mathbf{x}_t, \alpha), \quad (46)$$

which enables to write the first term in the RHS of (45)

$$\nabla_{\mathbf{x}}\mathbf{h}_\alpha(\mathbf{x}_t) \mathbf{F}(\mathbf{x}_t, \alpha) = \frac{d}{dt}\mathbf{h}_\alpha(\mathbf{x}_t) = \begin{pmatrix} \mathbf{f}(\mathbf{u}_t, \alpha) \\ \mathbf{A}_s(\mathbf{u}_t, \alpha) \mathbf{v}_t \\ \mathbf{A}_u(\mathbf{u}_t, \alpha) \mathbf{w}_t \end{pmatrix} = \tilde{\mathbf{F}}(\mathbf{h}_\alpha(\mathbf{x}_t)) \quad (47)$$

where

$$\tilde{\mathbf{F}} : \begin{pmatrix} \mathbf{u} \\ \mathbf{v} \\ \mathbf{w} \end{pmatrix} \mapsto \begin{pmatrix} \mathbf{f}(\mathbf{u}, \alpha) \\ \mathbf{A}_s(\mathbf{u}, \alpha) \mathbf{v} \\ \mathbf{A}_u(\mathbf{u}, \alpha) \mathbf{w} \end{pmatrix}. \quad (48)$$

Then, using the product rule of differentiation, the second and third term in (45) are

$$\begin{aligned}
& \boldsymbol{\xi}_t^\top \nabla_{\mathbf{x}}^2 \mathbf{h}_\alpha(\mathbf{x}_t) \mathbf{F}(\mathbf{x}_t, \alpha) + \nabla_{\mathbf{x}} \mathbf{h}_\alpha(\mathbf{x}_t) \mathbf{J}_t \boldsymbol{\xi}_t \\
&= \nabla_{\mathbf{x}} (\nabla_{\mathbf{x}} \mathbf{h}_\alpha(\mathbf{x}_t) \mathbf{F}(\mathbf{x}_t, \alpha)) \boldsymbol{\xi}_t \\
&= \nabla_{(u,v,w)} \left(\widehat{\mathbf{F}}(\mathbf{h}_\alpha(\mathbf{x}_t)) \right) \boldsymbol{\xi}_t \\
&= \begin{pmatrix} \nabla_{\mathbf{u}} \mathbf{f}(\mathbf{u}_t, \alpha) & 0 & 0 \\ \nabla_{\mathbf{u}} (\mathbf{A}_s(\mathbf{u}_t, \alpha) \mathbf{v}_t) & \mathbf{A}_s(\mathbf{u}_t, \alpha) & 0 \\ \nabla_{\mathbf{u}} (\mathbf{A}_u(\mathbf{u}_t, \alpha) \mathbf{w}_t) & 0 & \mathbf{A}_u(\mathbf{u}_t, \alpha) \end{pmatrix} \nabla_{\mathbf{x}} \mathbf{h}_\alpha(\mathbf{x}_t) \boldsymbol{\xi}_t \\
&= \begin{pmatrix} \nabla_{\mathbf{u}} \mathbf{f}(\mathbf{u}_t, \alpha) \boldsymbol{\xi}_t^u \\ \nabla_{\mathbf{u}} (\mathbf{A}_s(\mathbf{u}_t, \alpha) \mathbf{v}_t) \boldsymbol{\xi}_t^u + \mathbf{A}_s(\mathbf{u}_t, \alpha) \boldsymbol{\xi}_t^v \\ \nabla_{\mathbf{u}} (\mathbf{A}_u(\mathbf{u}_t, \alpha) \mathbf{w}_t) \boldsymbol{\xi}_t^u + \mathbf{A}_u(\mathbf{u}_t, \alpha) \boldsymbol{\xi}_t^w \end{pmatrix} \quad (49)
\end{aligned}$$

where $(\boldsymbol{\xi}_t^u, \boldsymbol{\xi}_t^v, \boldsymbol{\xi}_t^w)^\top := \nabla_{\mathbf{x}} \mathbf{h}_\alpha(\mathbf{x}_t) \boldsymbol{\xi}_t$. Finally, by substituting (47) and (49) into (45) we have,

$$\begin{aligned}
d\mathbf{h}_\alpha(\mathbf{X}_t) &= \begin{pmatrix} \mathbf{f}(\mathbf{u}_t, \alpha) \\ \mathbf{A}_s(\mathbf{u}_t, \alpha) \mathbf{v}_t \\ \mathbf{A}_u(\mathbf{u}_t, \alpha) \mathbf{w}_t \end{pmatrix} dt + \frac{1}{\sqrt{\Omega}} \begin{pmatrix} \nabla_{\mathbf{u}} \mathbf{f}(\mathbf{u}_t, \alpha) \boldsymbol{\xi}_t^u \\ \nabla_{\mathbf{u}} (\mathbf{A}_s(\mathbf{u}_t, \alpha) \mathbf{v}_t) \boldsymbol{\xi}_t^u + \mathbf{A}_s(\mathbf{u}_t, \alpha) \boldsymbol{\xi}_t^v \\ \nabla_{\mathbf{u}} (\mathbf{A}_u(\mathbf{u}_t, \alpha) \mathbf{w}_t) \boldsymbol{\xi}_t^u + \mathbf{A}_u(\mathbf{u}_t, \alpha) \boldsymbol{\xi}_t^w \end{pmatrix} dt \\
&\quad + \frac{1}{\sqrt{\Omega}} \nabla_{\mathbf{x}} \mathbf{h}_\alpha(\mathbf{X}_t) \mathbf{E}_t d\mathbf{B}_t + O(\Omega^{-1}). \quad (50)
\end{aligned}$$

From inspecting the form of (50), we conclude that

$$\mathbf{h}_\alpha(\mathbf{X}_t) = \begin{pmatrix} \mathbf{u}_t \\ \mathbf{v}_t \\ \mathbf{w}_t \end{pmatrix} + \frac{1}{\sqrt{\Omega}} \begin{pmatrix} \boldsymbol{\xi}_t^u \\ \boldsymbol{\xi}_t^v \\ \boldsymbol{\xi}_t^w \end{pmatrix} + O(\Omega^{-1}), \quad (51)$$

where $\mathbf{u}_t, \mathbf{v}_t, \mathbf{w}_t$ evolve according to (42) and $\boldsymbol{\xi}_t^u, \boldsymbol{\xi}_t^v, \boldsymbol{\xi}_t^w$ evolve according to the following system of linear SDEs

$$\begin{cases} d\boldsymbol{\xi}_t^u = \nabla_{\mathbf{u}} \mathbf{f}(\mathbf{u}_t, \alpha) \boldsymbol{\xi}_t^u dt + \mathbf{H}_t^u d\mathbf{B}_t, \\ d\boldsymbol{\xi}_t^v = (\nabla_{\mathbf{u}} (\mathbf{A}_s(\mathbf{u}_t, \alpha) \mathbf{v}_t) \boldsymbol{\xi}_t^u + \mathbf{A}_s(\mathbf{u}_t, \alpha) \boldsymbol{\xi}_t^v) dt + \mathbf{H}_t^v d\mathbf{B}_t, \\ d\boldsymbol{\xi}_t^w = (\nabla_{\mathbf{u}} (\mathbf{A}_u(\mathbf{u}_t, \alpha) \mathbf{w}_t) \boldsymbol{\xi}_t^u + \mathbf{A}_u(\mathbf{u}_t, \alpha) \boldsymbol{\xi}_t^w) dt + \mathbf{H}_t^w d\mathbf{B}_t, \end{cases} \quad (52)$$

with

$$\begin{bmatrix} \mathbf{H}_t^u \\ \mathbf{H}_t^v \\ \mathbf{H}_t^w \end{bmatrix} := \nabla_{\mathbf{x}} \mathbf{h}_\alpha(\mathbf{x}_t) \mathbf{E}_t. \quad (53)$$

S4 Numerical Investigations

In this section, we give further details related to the numerical investigations included in Section 6. In particular, we provide the details of the systems used and additional comparisons between SSA and pLNA.

S4.1 The NF- κ B reaction network

The NF- κ B network consists of 11 species detailed in Table S2.

Table S2: Details of the 11 species characterising the NF- κ B network and their initial concentrations in three simulation settings with different value of the bifurcation parameter.

	Name	Description	Initial values Fig. S9	Initial values Fig. S10	Initial values Fig. S11
1	N_c	Free Cytoplasmic NF κ B	0.0059	0.0065	0.0044
2	I_c	Free Cytoplasmic I κ Ba	0.0119	0.0289	0.0267
3	NI_c	Cytoplasmic NF κ B-I κ Ba	0.0096	0.0611	0.0442
4	N_n	Free nuclear NF κ B	0.0639	0.0111	0.0305
5	I_n	Free nuclear I κ Ba	0.0001	0.0010	0.0003
6	NI_n	Nuclear NF κ B-I κ Ba	0.0002	0.0005	0.0005
7	I_m	I κ Ba transcription	0.0001	0.0002	0.0002
8	K_n	Kinase IKKn	0.0368	0.0071	0.0015
9	K_a	Kinase IKKa	0.0083	0.0034	0.0023
10	A_m	A20 transcription	0.0001	0.0001	0.0001
11	A	A20	0.0117	0.0139	0.0135

Table S3: The parameters of NF- κ B system and the values used in simulations. Each of the three different levels of TNF α displayed in last row are used for the simulations in Figures S9,S10,S11, respectively.

parameter	description	value	unit
k_v	Cytoplasm:Nucleus ratio	3.3	–
k_p	IKK α production	0.0006	s^{-1}
k_a	Activation caused by TNF α	0.004	s^{-1}
k_i	Spontaneous IKK activation	0.003	s^{-1}
k_{a1a}	NF κ B-I κ B α association	0.5	$\mu M^{-1} s^{-1}$
k_{d1a}	NF κ B-I κ B α dissociation	0.0005	s^{-1}
k_{c1a}	Catalysis of IKK-I κ B α dimer	0.074	s^{-1}
k_{c2a}	Catalysis of IKK-I κ B α -NF κ B trimer	0.37	s^{-1}
k_{t2a}	degradation of I κ B α (IKK dependent)	0.1	s^{-1}
c_{4a}	Free I κ B α degradation	0.0005	s^{-1}
c_{5a}	NF κ B complexed I κ B α degradation	0.000022	s^{-1}
k_{i1}	NF κ B nuclear import	0.0026	s^{-1}
k_{e1}	NF κ B nuclear export	0.000052	s^{-1}
k_{e2a}	NF κ B-I κ B α nuclear export	0.01	s^{-1}
k_{i3a}	I κ B α nuclear import	0.00067	s^{-1}
k_{e3a}	I κ B α nuclear export	0.000335	s^{-1}
h	Order of hill function	2	–
k	Hill constant	0.0650	$\mu M/L$
c_{1a}	I κ B α mRNA synthesis	1.400e-07	$\mu M^{-1} s^{-1}$
c_{2a}	I κ B α translation rate	0.5	s^{-1}
c_{3a}	I κ B α mRNA degradation	0.0003	s^{-1}
c_1	I κ B α mRNA synthesis	1.4e-07	$\mu M^{-1} s^{-1}$
c_2	A20 mRNA translation	0.5	s^{-1}
c_3	A20 mRNA degradation	0.00048	s^{-1}
c_4	A20 degradation	0.0045	s^{-1}
$k_{b,A20}$	Half-max A20 inhibition concentration	0.0018	$\mu M/L$
TNF- κ B	total NF- κ B concentration	0.08	μM
TIKK	total IKK concentration	0.08	μM
TNF α	Tumor necrosis factor alpha level	1.5 / 3.66 / 10	ng/mL

The ODE system for the NF- κ B system are given in table S4

Table S4: The RRE ODE system equations for the NF- κ B system in [4]

\dot{N}_c	$= k_{d1a}NI_c - k_{a1a}N_cI_c - k_{i1}N_c + c_{5a}NI_c + k_vk_{e1}N_n + k_{t2a} \times (TNFKB - N_c - NI_c - N_n + NI_n)$
\dot{I}_c	$= k_{d1a}NI_c - k_{a1a}N_cI_c - k_{i3a}I_c + k_vk_{e3a}I_n - c_{4a}I_c + c_{2a}I_m - k_{c1a}K_aI_c$
\dot{NI}_c	$= k_{a1a}N_cI_c - k_{d1a}NI_c + k_vk_{e2a}NI_n - c_{5a}NI_c - k_{c2a}K_aNI_c$
\dot{N}_n	$= k_{d1a}NI_n - k_vk_{a1a}N_nI_n + k_{i1}N_c - k_vk_{e1}N_n$
\dot{I}_n	$= k_{d1a}NI_n - k_vk_{a1a}N_nI_n + k_{i3a}I_c - k_vk_{e3a}I_n - c_{4a}I_n$
\dot{NI}_n	$= k_vk_{a1a}NI_n - k_{d1a}NI_n - k_vk_{e2a}NI_n$
\dot{I}_m	$= c_{1a}(N_n^h/(N_n^h + (k/k_v)^h)) - c_{3a}I_m$
\dot{K}_n	$= k_p(TIKK - K_n - K_a)(k_{bA20}/(k_{bA20} + A \times TNF\alpha/10)) - k_aTNF\alpha K_n/10$
\dot{K}_a	$= k_aTNF\alpha K_n/10 - k_iK_a$
\dot{A}_m	$= c_1(N_n^h/(N_n^h + (k/k_v)^h)) - c_3A_m$
\dot{A}	$= c_2A_m - c_4A$

The propensity functions used for the SSA are provided in Table S4.1. The values of the parameters are the same as in Table S3 with suitable rate constant conversions applied.

Table S5: NF- κ B reactions and the corresponding propensity functions used for the SSA simulations of the NF- κ B system.

reaction	rate
$N_c + I_c \xrightarrow{k_{a1a}} NI_c$	$k_{a1a} \times I_c \times N_c / \Omega$
$NI_c \xrightarrow{k_{d1a}} N_c + I_c$	$k_{d1a} \times NI_c$
$N_n + I_n \xrightarrow{k_{a1a}} NI_n$	$k_v k_{a1a} \times I_n \times N_n / \Omega$
$NI_n \xrightarrow{k_{d1a}} N_n + I_n$	$k_{d1an} \times NI_n$
$K_a + I_c \xrightarrow{k_{c1a}} K_a + I_p$	$k_{c1a} \times K_a \times I_c / \Omega$
$K_a + NI_c \xrightarrow{k_{c2a}} K_a + NI_p$	$k_{c2a} \times K_a \times NI_c / \Omega$
$NI_p \xrightarrow{k_{t2a}} N_c$	$k_{t2a} \times NI_p$
$N_c \xrightarrow{k_{i1}} N_n$	$k_{i1} \times N_c$
$N_n \xrightarrow{k_{e1}} N_c$	$k_{e1} \times k_v \times N_n$
$NI_n \xrightarrow{k_{e2a}} NI_c$	$k_{e2a} \times k_v \times NI_n$
$I_c \xrightarrow{k_{i3a}} I_n$	$k_{i3a} \times I_c$
$I_n \xrightarrow{k_{e3a}} I_c$	$k_{e3a} \times k_v \times I_c$
$\emptyset \xrightarrow{H_I} I_m$	$(c_{1a}\Omega) \frac{N_n^h}{N_n^h + (k\Omega/k_v)^h}$
$I_m \xrightarrow{c_{2a}} I_m + I_c$	$c_{2a} \times I_m$
$I_m \xrightarrow{c_{3a}} \emptyset$	$c_{3a} \times I_m$
$I_c \xrightarrow{c_{4a}} \emptyset$	$c_{4a} \times I_c$
$I_n \xrightarrow{c_{4a}} \emptyset$	$c_{4a} \times I_n$
$NI_c \xrightarrow{c_{5a}} N_c$	$c_{5a} \times NI_c$
$\emptyset \xrightarrow{H_A} A_m$	$(c_1\Omega) \frac{N_n^h}{N_n^h + (k\Omega/k_v)^h}$
$A_m \xrightarrow{c_2} A_m + A$	$c_2 \times A_m$
$A_m \xrightarrow{c_3} \emptyset$	$c_3 \times A_m$
$A \xrightarrow{c_4} \emptyset$	$c_4 \times A$
$K_i \xrightarrow{M_A} K_n$	$k_p(TIKK - K_n - K_a) \frac{k_{b,A20} \times \Omega}{(k_{b,A20}\Omega) + A \times TNF\alpha/10}$
$K_n \xrightarrow{TNF\alpha/10 \times k_a} K_a$	$TNF\alpha/10 \times k_a \times K_n$
$K_a \xrightarrow{k_i} K_i$	$k_i \times K_a$

S4.1.1 Details for Figure 8

The bifurcation parameter of this system is the level of the Tumor necrosis factor alpha level (TNF α). The Hopf bifurcation value is $\approx 3.66ng/mL$. The simulations in Figure 8 are produced with the level of TNF α at the Hopf bifurcation value and with initial conditions given in Table S2 in the column “Initial values Fig. S10”.

The empirical density functions of the probability distribution of each variable are derived using the kernel density function “ksdensity” in MATLAB [27]. To ensure good visibility of all the curves, we scale them. Specifically, both the x - and z -axis range from 0 to 1 since we divide both the value of each variable and their densities obtained for both SSA and pcLNA by their maximum observed values for both algorithms.

S4.1.2 Further numerical investigations for the NF- κ B system

See caption of Figures S9, S10, S11 for more details on additional comparisons for this system, in the cases where the parameter values give a system that presents a stable focus (see Figure S9), the case where the parameter values are exactly on the Hopf bifurcation point (see Figure S10), and the case where a limit cycle appears (see Figure S11).

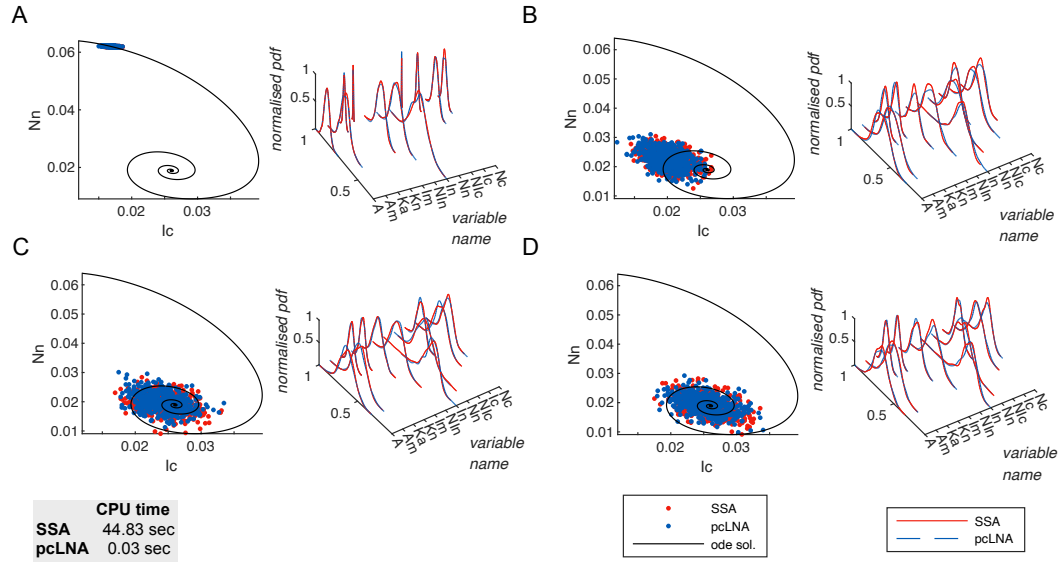


Figure S9: Comparison between SSA (red) and pcLNA (blue) for the NF- κ B system at $\Omega = 600,000$ with $\text{TNF}\alpha$ level = 1.5 ng/mL. Panels (A)–(D) correspond to times $t = 5, \tau + 5, 2\tau + 5, 3\tau + 5$, where $\tau \approx 102.095$ is the oscillation period. Each panel shows (left) the states recorded at time t of the simulations with solutions of the corresponding RRE, and (right) the corresponding empirical probability density functions of each system variable. Initial conditions and parameter values are given in Tables S2 and S3.

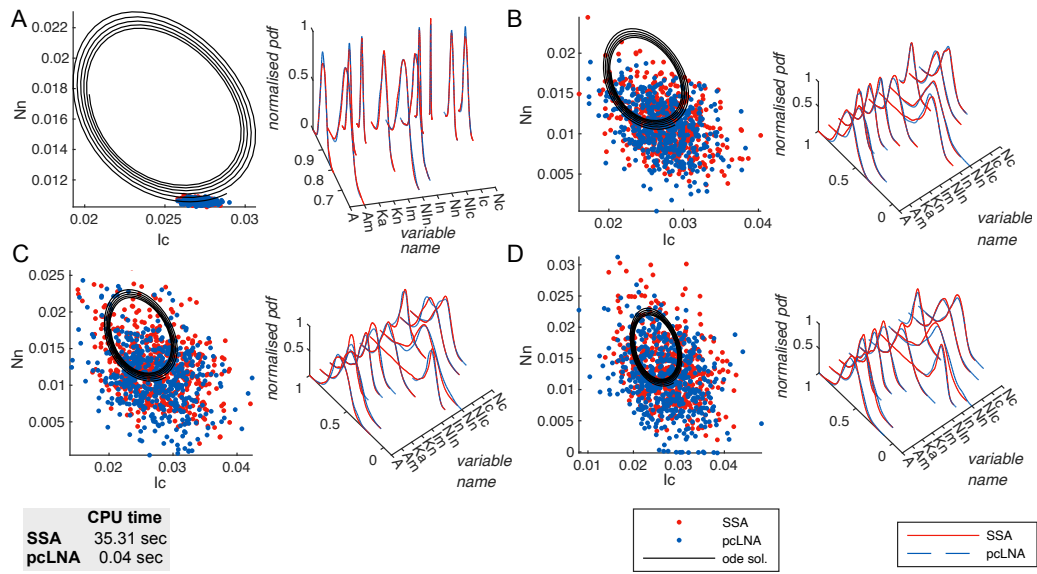


Figure S10: Comparison between SSA (red) and pcLNA (blue) for the NF- κ B system at $\Omega = 600,000$ with TNF α level = 3.66 ng/mL (Hopf bifurcation point). Panels (A)–(D) correspond to times $t = 5, \tau + 5, 2\tau + 5, 3\tau + 5$, where $\tau \approx 102.095$ is the oscillation period. Each panel shows (left) the states recorded at time t of the simulations with solutions of the corresponding RRE, and (right) the corresponding empirical probability density functions of each system variable. Initial conditions and parameter values are provided in Tables S2 and S3.

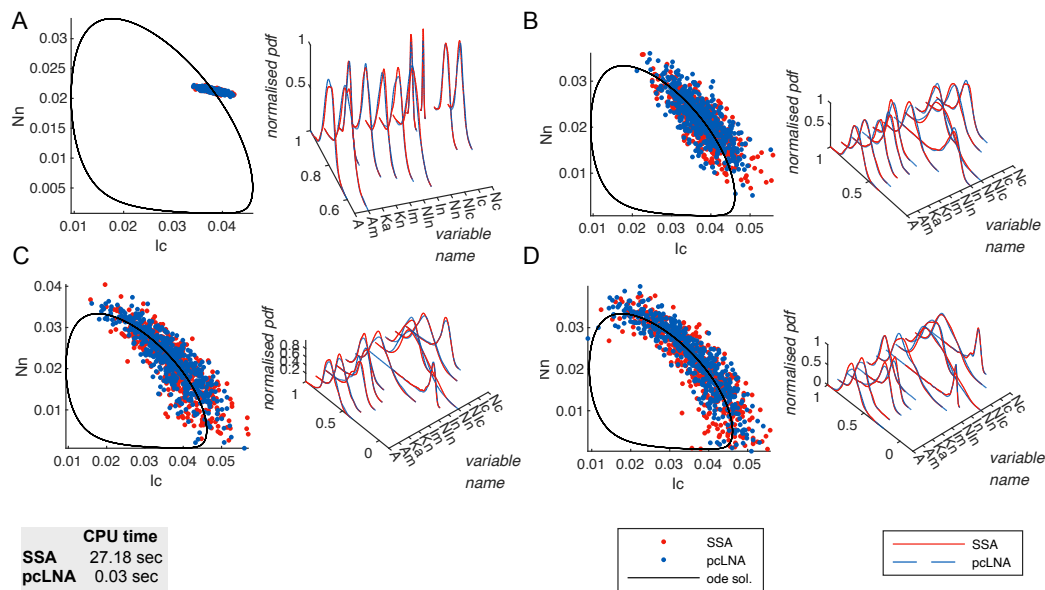


Figure S11: Comparison between SSA (red) and pcLNA (blue) for the NF- κ B system at $\Omega = 600,000$ with TNF α level = 10 ng/mL. Panels (A)–(D) correspond to times $t = 5, \tau + 5, 2\tau + 5, 3\tau + 5$, where $\tau \approx 102.095$ is the oscillation period. Each panel shows (left) the states recorded at time t of the simulations with solutions of the corresponding RRE, and (right) the corresponding empirical probability density functions of each system variable. Initial conditions and parameter values are listed in Tables S2 and S3.

S4.2 The Brusselator reaction network

The two dimensional Brusselator network, introduced in [39], consists of two chemical species, A and B , which undergo the following reactions,



If, for each $t \geq 0$, we let $\mathbf{Y}(t) = (Y_1(t), Y_2(t))^\top$ denote the number of molecules of A and B respectively, then these reactions occur according to the following intensities

$$\pi_1 = \Omega, \quad \pi_2 = Y_1, \quad \pi_3 = bY_1, \quad \pi_4 = cY_1^2 Y_2 / \Omega^2.$$

With system size Ω and $\mathbf{X}(t) = \mathbf{Y}(t)/\Omega$ for each $t \geq 0$, the corresponding RRE solution in the $\Omega \rightarrow \infty$ limit is

$$\begin{cases} \dot{x}_1 = 1 - x_1(1 + b - cx_1x_2), \\ \dot{x}_2 = x_1(b - cx_1x_2). \end{cases} \quad (54)$$

From studying the Jacobian matrix of (54), we may conclude the system has a non-hyperbolic equilibrium at $(x_1, x_2) = (1, 2)^\top$, when $b = 2$ and $c = 1$, with purely imaginary conjugate eigenvalues $\pm i$. Through small deviations of b we deduce the Hopf bifurcation is supercritical with losses of stability occurring as the eigenvalues cross the imaginary axis. Parameters $b < 2$ give rise to a stable equilibrium, whereas $b > 2$ gives rise to an unstable equilibrium surrounded by a unique and stable limit cycle.

Table S6: Species in the Brusselator network and their initial concentrations for three different values of parameter b .

	Name	Description	Initial values Fig. S12	Initial values Fig. S13	Initial values Fig. S14
1	A	Chemical species A	0.8000	0.8000	1.0340
2	B	Chemical species B	1.5000	1.5000	2.9230

Table S7: Parameters used in the Brusselator network.

Parameter	Description	Value	Unit
c	Catalytic reaction rate	1	$\mu M^{-2} s^{-1}$
b	Conversion rate of A to B	1.7 / 2.0 / 2.3	s^{-1}

Table S8: The RRE ODEs for the mean-field dynamics of the Brusselator in the limit $\Omega \rightarrow \infty$.

$$\begin{aligned} \dot{x}_1 &= 1 - x_1(1 + b - cx_1x_2) \\ \dot{x}_2 &= x_1(b - cx_1x_2) \end{aligned}$$

Table S9: Brusselator reactions and their corresponding propensity functions for SSA simulations.

Reaction	Propensity function
$\emptyset \xrightarrow{1} A$	$\pi_1 = \Omega$
$A \xrightarrow{1} \emptyset$	$\pi_2 = Y_1$
$A \xrightarrow{b} B$	$\pi_3 = bY_1$
$2A + B \xrightarrow{c} 3A$	$\pi_4 = cY_1^2Y_2/\Omega^2$

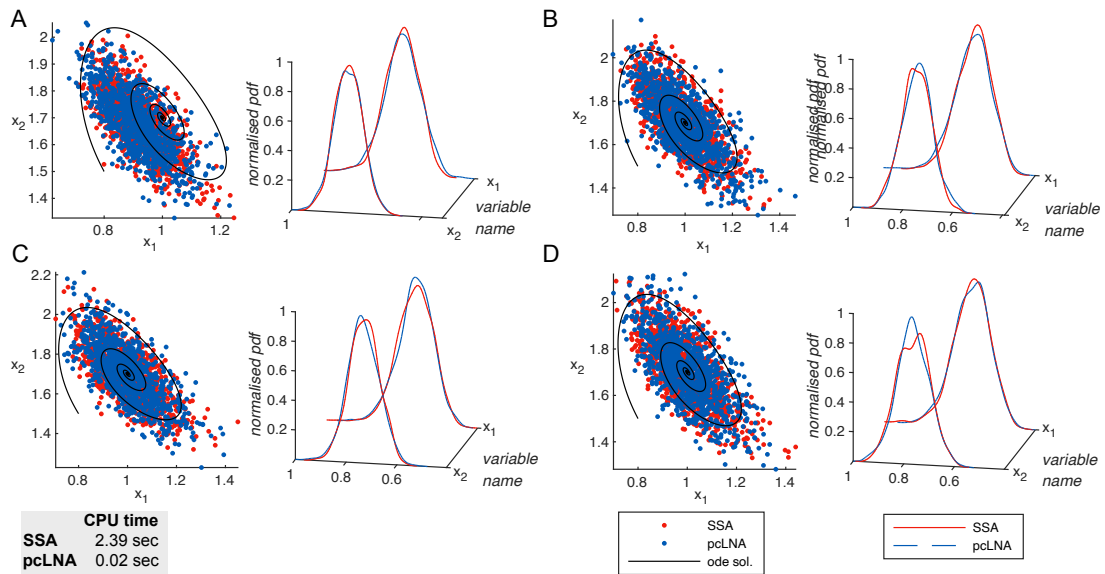


Figure S12: Comparison between SSA (red) and pcLNA (blue) for the Brusselator system at $\Omega = 1000$ with parameter $b = 1.7$. Panels (A)–(D) correspond to times $t = \tau + 0.5$, $3\tau + 0.5$, $5\tau + 0.5$, $7\tau + 0.5$ with period $\tau = 6.2919$. Each panel shows (left) the states recorded at time t of the simulations with solutions of the corresponding RRE, and (right) the corresponding empirical probability density functions of each system variable. Initial conditions and parameter values are given in Tables S6 and S7.

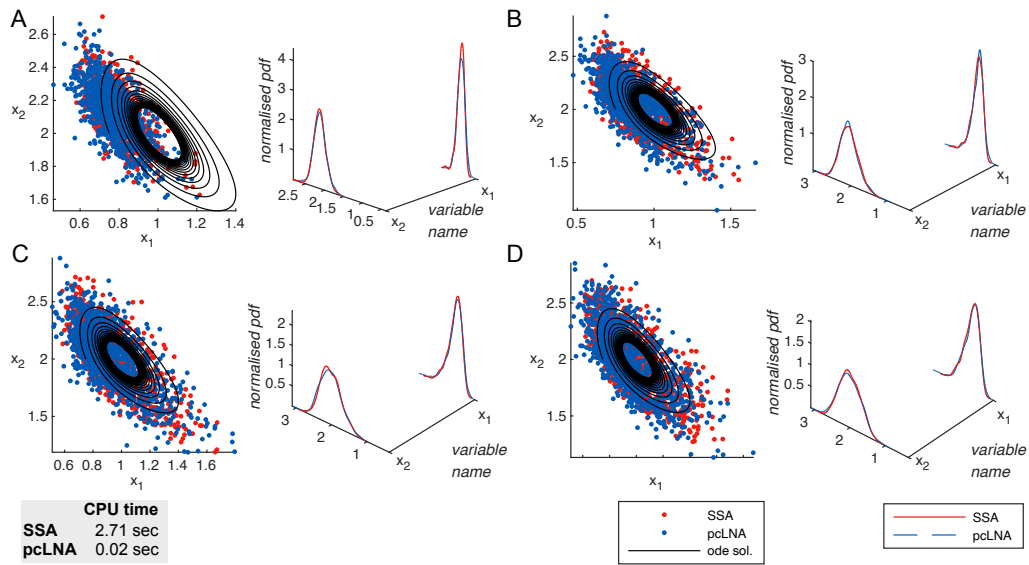


Figure S13: Comparison between SSA (red) and pcLNA (blue) for the Brusselator system at $\Omega = 1000$ with parameter $b = 2$. Panels (A)–(D) correspond to times $t = \tau + 0.5$, $3\tau + 0.5$, $5\tau + 0.5$, $7\tau + 0.5$ with period $\tau = 6.35$. Each panel shows (left) the states recorded at time t of the simulations with solutions of the corresponding RRE, and (right) the corresponding empirical probability density functions of each system variable. Initial conditions and parameter values are provided in Tables S6 and S7.

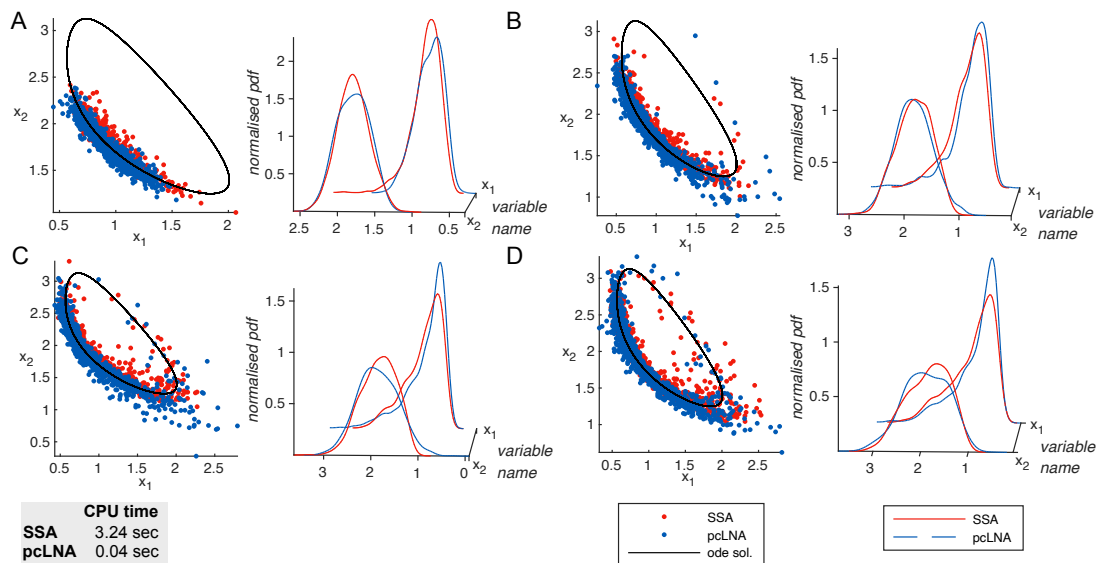


Figure S14: Comparison between SSA (red) and pcLNA (blue) for the Brusselator system at $\Omega = 1000$ with parameter $b = 2.3$. Panels (A)–(D) correspond to times $t = \tau + 0.5$, $3\tau + 0.5$, $5\tau + 0.5$, $7\tau + 0.5$ with period $\tau = 6.4276$. Each panel shows (left) the states recorded at time t of the simulations with solutions of the corresponding RRE, and (right) the corresponding empirical probability density functions of each system variable. Initial conditions and parameter values are listed in Tables S6 and S7.

S4.3 The smallest Hopf bifurcation reaction network

The system is described in [71]. The tables S10, S11, S12, S13 describe the species and their initial conditions, the parameters, the ODE system, and the propensity functions of the SSA simulations of this system, respectively. The results in Figures S15, S16, and S17 are derived using the same method as used for Figure 3 in the main paper. The bifurcation parameter is k_1 and its value at bifurcation is 6.6. The computation of the empirical density functions is done as described in SI section S4.1.1. We used 1000 trajectories of each simulation algorithm to produce the results.

Table S10: Species in the smallest Hopf bifurcation network and their initial concentrations for three different values of parameter k_1 .

	Name	Description	Initial values Fig. S15	Initial values Fig. S16	Initial values Fig. S17
1	X_1	Species 1	3.8220	3.8220	2.4460
2	X_2	Species 2	3.8460	3.8460	1.0720
3	X_3	Species 3	5.1400	5.1400	1.2940

Table S11: Parameters used in the smallest Hopf bifurcation network.

Parameter	Description	Value	Unit
k_1	Activation rate	6 / 6.6 / 7	s^{-1}
k_2	Interaction rate between X_1 and X_2	2.2	s^{-1}
k_3	Degradation rate of X_2	2.2	s^{-1}
k_4	Conversion rate from X_1 to X_3	2.2	s^{-1}
k_5	Conversion rate from X_3 to X_2	2.2	s^{-1}
A	External activation strength	1	–

Table S12: The RRE ODEs for the mean-field dynamics of the smallest Hopf bifurcation network in the limit $\Omega \rightarrow \infty$.

$$\begin{aligned} \dot{x}_1 &= k_1 A x_1 - k_4 x_1 - k_2 x_1 x_2 \\ \dot{x}_2 &= -k_3 x_2 + k_5 x_3 \\ \dot{x}_3 &= k_4 x_1 - k_5 x_3 \end{aligned}$$

Table S13: smallest Hopf bifurcation reactions and their corresponding propensity functions for SSA simulations.

Reaction	Propensity function
$X_1 \xrightarrow{k_1 A} X_1$	$\pi_1 = k_1 A Y_1$
$X_1 + X_2 \xrightarrow{k_2} \emptyset$	$\pi_2 = k_2 \cdot Y_1 \cdot Y_2 / \Omega$
$X_2 \xrightarrow{k_3} \emptyset$	$\pi_3 = k_3 \cdot Y_2$
$X_1 \xrightarrow{k_4} X_3$	$\pi_4 = k_4 \cdot Y_1$
$X_3 \xrightarrow{k_5} X_2$	$\pi_5 = k_5 \cdot Y_3$

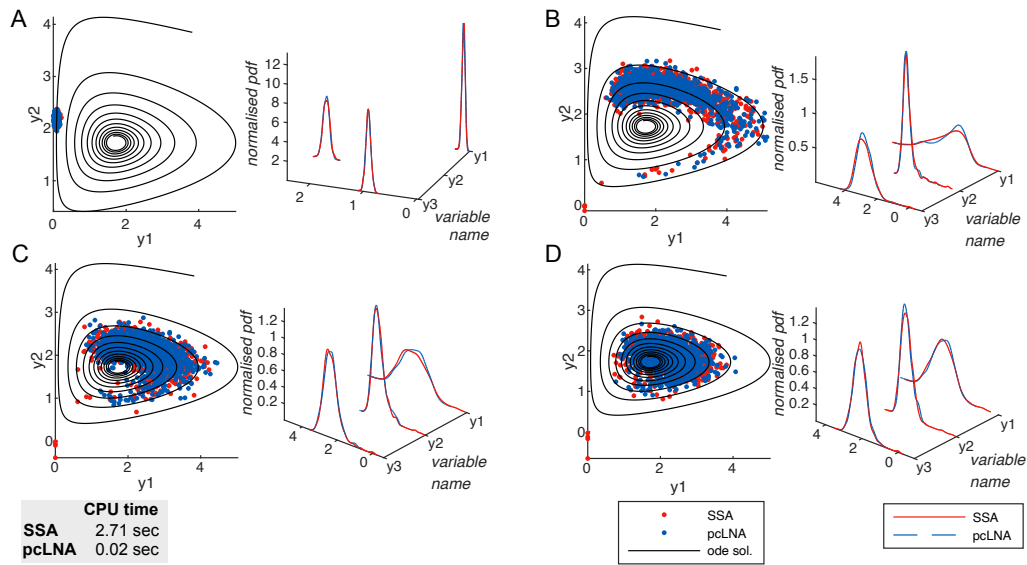


Figure S15: Comparison between SSA (red) and pcLNA (blue) for the smallest Hopf bifurcation network at $\Omega = 500$ with parameter $k_1 = 6$. Panels (A)–(D) correspond to times $t = \tau + 1$, $3\tau + 1$, $5\tau + 1$, $7\tau + 1$ with period $\tau \approx 3$. Each panel shows (left) the states recorded at time t of the simulations with solutions of the corresponding RRE, and (right) the corresponding empirical probability density functions of each system variable. Initial conditions and parameter values are given in Tables S10 and S11.

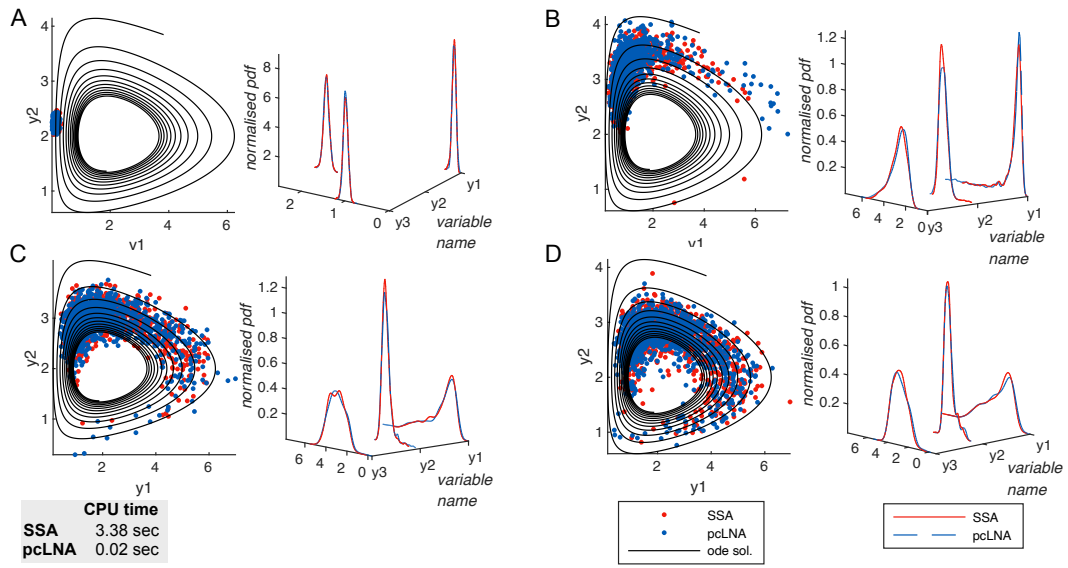


Figure S16: Comparison between SSA (red) and pcLNA (blue) for the smallest Hopf bifurcation network at $\Omega = 500$ with parameter $k_1 = 6.6$. Panels (A)–(D) correspond to times $t = \tau + 1$, $3\tau + 1$, $5\tau + 1$, $7\tau + 1$ with period $\tau \approx 3$. Each panel shows (left) the states recorded at time t of the simulations with solutions of the corresponding RRE, and (right) the corresponding empirical probability density functions of each system variable. Initial conditions and parameter values are provided in Tables S10 and S11.

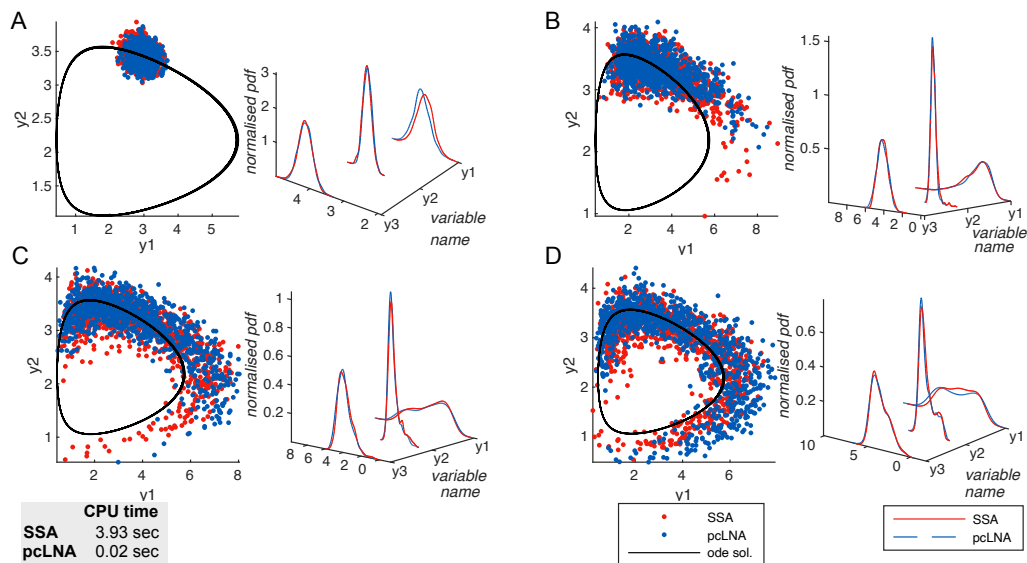


Figure S17: Comparison between SSA (red) and pcLNA (blue) for the smallest Hopf bifurcation network at $\Omega = 500$ with parameter $k_1 = 7$. Panels (A)–(D) correspond to times $t = \tau + 1$, $3\tau + 1$, $5\tau + 1$, $7\tau + 1$ with period $\tau \approx 3$. Each panel shows (left) the states recorded at time t of the simulations with solutions of the corresponding RRE, and (right) the corresponding empirical probability density functions of each system variable. Initial conditions and parameter values are listed in Tables S10 and S11.

S4.4 The genetic toggle switch reaction network

The system is described in [14]. The tables S14, S15, S16, S17 describe the species and their initial conditions, the parameters, the ODE system, and the propensity functions of the SSA simulations of this system, respectively. The results in Figure S18 are derived using the same method as used for Figure 3 in the main paper. The computation of the empirical density functions is done as described in SI section S4.1.1. We used 1000 trajectories of each simulation algorithm to produce the results.

The results in Figure S19 are derived using the same method as used for Figure 3 in the main paper, except for the LNA simulation where the Algorithm is again Algorithm 3 in the main paper except omitting the steps A and C.3 (i.e. no phase correction is applied). The computation of the empirical density functions is done as described in SI section S4.1.1. We used 1000 trajectories of each simulation algorithm to produce the results.

Table S14: Species in the genetic toggle switch network and their initial concentrations.

	Name	Description	Initial values	
			ODE solution 1 Fig. S18	ODE solution 2 Fig. S18
1	x_1	Repressor 1	0.3067	0.4311
2	x_2	Repressor 2	0.4311	0.3067

Table S15: Parameters used in the genetic toggle switch network.

Parameter	Description	Value	Unit
a_1	Activation rate of x_1	1.5	s^{-1}
a_2	Activation rate of x_2	1.5	s^{-1}
b	Hill coefficient for x_2 regulation of x_1	4	–
g	Hill coefficient for x_1 regulation of x_2	4	–
A	External activation strength	1	–

Table S16: The RRE ODEs for the mean-field dynamics of the genetic toggle switch in the limit $\Omega \rightarrow \infty$.

$$\begin{aligned} \dot{x}_1 &= \frac{a_1 A}{1+x_2^b} - x_1 \\ \dot{x}_2 &= \frac{a_2}{1+x_1^g} - x_2 \end{aligned}$$

Table S17: genetic toggle switch reactions and their corresponding propensity functions for SSA simulations.

Reaction	Propensity function
$X_1 \xrightarrow{a_1 A} X_1$	$\pi_1 = \frac{a_1 A \Omega}{1+Y_2^b}$
$X_1 \rightarrow \emptyset$	$\pi_2 = Y_1$
$X_2 \xrightarrow{a_2} X_2$	$\pi_3 = \frac{a_2 \Omega}{1+Y_1^g}$
$X_2 \rightarrow \emptyset$	$\pi_4 = Y_2$

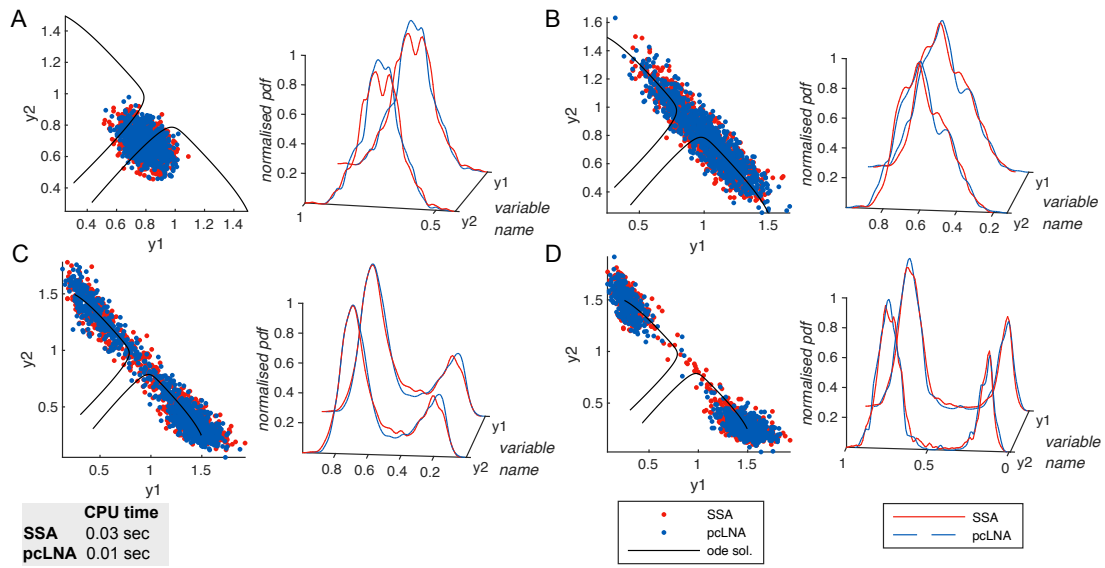


Figure S18: Comparison between SSA (red) and pcLNA (blue) for the genetic toggle switch network at $\Omega = 100$. Panels (A)–(D) correspond to times $t = 0.5006, 2.0024, 5.0059, 9.5051$, respectively. Each panel shows (left) the states recorded at time t of the simulations with solutions of the corresponding RRE, and (right) the corresponding empirical probability density functions of each system variable. The initial conditions for the two ODE solutions are provided in Table S14, and the parameter values are given in Table S15.

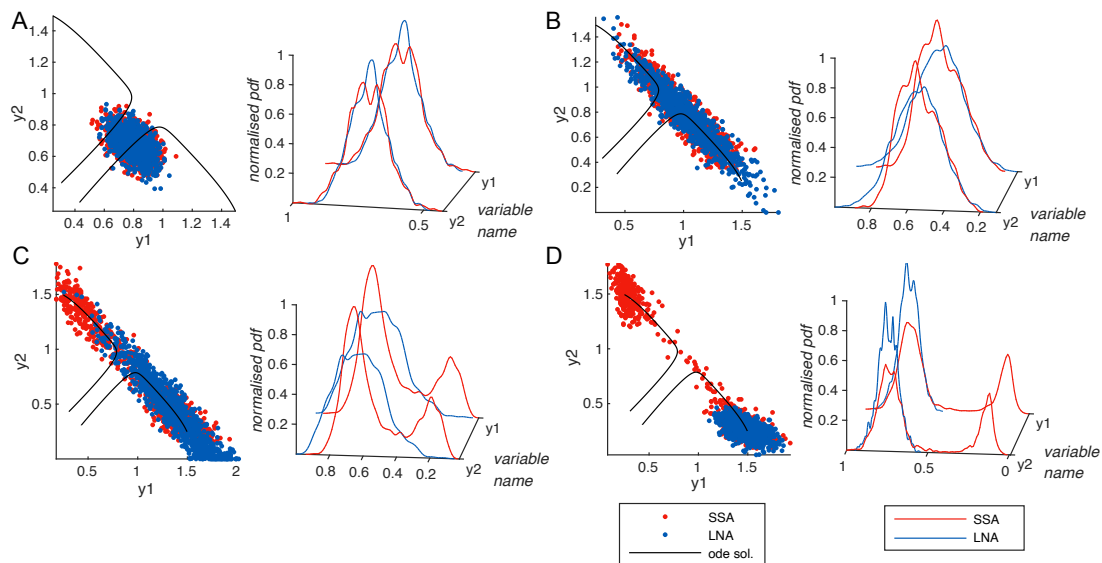


Figure S19: Comparison between SSA (red) and (standard) LNA (blue) for the genetic toggle switch network at $\Omega = 100$. Panels (A)–(D) correspond to times $t = 0.5006, 2.0024, 5.0059, 9.5051$, respectively. Each panel shows (left) the states recorded at time t of the simulations with solutions of the corresponding RRE, and (right) the corresponding empirical probability density functions of each system variable. The initial conditions for the two ODE solutions are provided in Table S14, and the parameter values are given in Table S15.

S4.5 The cell cycle reaction network

The system is described in [2]; see section “A Two-Variable Example: The Cdc2-Cyclin B/Wee1 System”. The tables S18, S19, S20, S21 describe the species and their initial conditions, the parameters, the ODE system, and the propensity functions of the SSA simulations of this system, respectively. The results in Figure S20 are derived using the same method as used for Figure 3 in the main paper. The computation of the empirical density functions is done as described in SI section S4.1.1. We used 1000 trajectories of each simulation algorithm to produce the results.

Table S18: Species in the cell cycle network and their initial concentrations.

	Name	Description	Initial values	
			ODE solution 1 Fig. S20	ODE solution 2 Fig. S20
1	x_1	Cdc2-Cyclin B	0.9300	0.8400
2	y_1	Wee1	0.9100	0.9900

Table S19: Parameters used in the cell cycle network.

Parameter	Description	Value	Unit
a_1	Production rate of x_1	1	s^{-1}
a_2	Production rate of y_1	1	s^{-1}
b_1	Hill coefficient for y_1 regulation of x_1	200	–
b_2	Hill coefficient for x_1 regulation of y_1	10	–
γ_1	Hill exponent for y_1 regulation of x_1	4	–
γ_2	Hill exponent for x_1 regulation of y_1	4	–
K_1	Half-activation constant for x_1 regulation of y_1	2.3403	–
K_2	Half-activation constant for y_1 regulation of x_1	1	–
A	External activation strength	1	–

Table S20: The RRE ODEs for the mean-field dynamics of the cell cycle system in the limit $\Omega \rightarrow \infty$.

$$\begin{aligned} \dot{x}_1 &= a_1 - a_1 x_1 - \frac{b_1 x_1 ((A y_1)^{\gamma_1})}{K_1^{\gamma_1} + (A y_1)^{\gamma_1}} \\ \dot{y}_1 &= a_2 - a_2 y_1 - \frac{b_2 y_1 (x_1^{\gamma_2})}{K_2^{\gamma_2} + x_1^{\gamma_2}} \end{aligned}$$

Table S21: cell cycle reactions and the corresponding propensity functions for SSA simulations.

Reaction	Propensity function
$X_1 \xrightarrow{a_1} X_1$	$\pi_1 = a_1 \cdot \Omega$
$X_1 \rightarrow \emptyset$	$\pi_2 = Y_1$
$X_2 \xrightarrow{b_1} X_2$	$\pi_3 = \frac{b_1 Y_1 ((A Y_2)^{\gamma_1})}{(K_1 \Omega)^{\gamma_1} + (A Y_2)^{\gamma_1}}$
$X_2 \rightarrow \emptyset$	$\pi_4 = Y_2$
$Y_1 \xrightarrow{a_2} Y_1$	$\pi_5 = a_2 \cdot \Omega$
$Y_1 \rightarrow \emptyset$	$\pi_6 = Y_2$
$Y_2 \xrightarrow{b_2} Y_2$	$\pi_7 = \frac{b_2 Y_2 ((Y_1)^{\gamma_2})}{(K_2 \Omega)^{\gamma_2} + (Y_1)^{\gamma_2}}$
$Y_2 \rightarrow \emptyset$	$\pi_8 = Y_3$

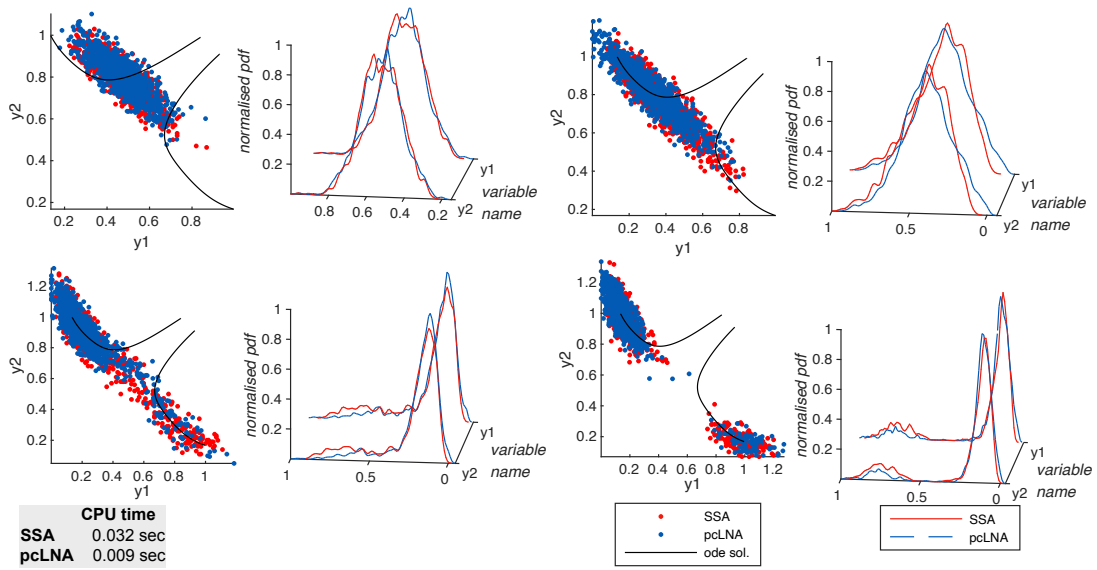


Figure S20: Comparison between SSA (red) and pcLNA (blue) for the cell cycle network at $\Omega = 100$. Panels (A)–(D) correspond to times $t = 0.5000, 9.9999, 49.9996, 100.0000$, respectively. Each panel shows (left) the states recorded at time t of the simulations with solutions of the corresponding RRE, and (right) the corresponding empirical probability density functions of each system variable. The initial conditions for the two ODE solutions are provided in Table S18, and the parameter values are given in Table S19.

S4.6 The somitogenesis switch reaction network

The system is described in [21]. The tables S22, S23, S24, S25 describe the species and their initial conditions, the parameters, the ODE system, and the propensity functions of the SSA simulations of this system, respectively. The results in Figure S21 are derived using the same method as used for Figure 3 in the main paper. The computation of the empirical density functions is done as described in SI section S4.1.1. We used 1000 trajectories of each simulation algorithm to produce the results.

Table S22: Species in the somitogenesis switch network and their initial concentrations.

	Name	Description	Initial values ODE solution 1 Fig. S21	Initial values ODE solution 2 Fig. S21
1	R	Retinoic Acid (RA)	1.1500	1.2000
2	M_C	cyp26 mRNA	1.7467	1.7067
3	C	CYP26 protein	6.2333	6.0900
4	F	FGF8 protein	0.4933	0.4800

Table S23: Parameters used in the somitogenesis switch network.

Parameter	Description	Value	Unit
k_{s1}	RA synthesis rate via RALDH2	1	s^{-1}
RALDH2	RA synthetase concentration	7.1	–
k_{d1}	RA degradation via CYP26	1	s^{-1}
k_{d5}	Basal RA degradation	0	s^{-1}
V_0	Basal transcription of M_C	0.365	s^{-1}
V_{sc}	Activated transcription of M_C	7.1	s^{-1}
K_a	Activation constant for M_C production	0.5	–
n	Hill coefficient for FGF activation of M_C	2	–
k_{d3}	mRNA degradation rate	1	s^{-1}
k_{s2}	Translation rate of CYP26	1	s^{-1}
k_{d2}	CYP26 degradation rate	0.28	s^{-1}
k_{s3}	FGF8 synthesis rate	1	s^{-1}
M_0	Baseline activator level for FGF synthesis	5	–
K_I	Inhibition constant for RA effect on FGF	0.5	–
m	Hill coefficient for RA inhibition of FGF	2	–
k_{d4}	FGF degradation rate	1	s^{-1}
L	Normalization constant for spatial scaling	50	–
A	External activation strength	1	–

Table S24: The RRE ODEs for the mean-field dynamics of the somitogenesis switch in the limit $\Omega \rightarrow \infty$.

$$\begin{aligned}
 \dot{R} &= k_{s1} \cdot \text{RALDH2} - k_{d1}RC - k_{d5}R \\
 \dot{M}_C &= V_0 + \frac{V_{sc}F^n}{K_a^n + F^n} - k_{d3}M_C \\
 \dot{C} &= k_{s2}M_C - k_{d2}C \\
 \dot{F} &= k_{s3} \cdot \frac{M_0A/L \cdot K_I^m}{K_I^m + R^m} - k_{d4}F
 \end{aligned}$$

Table S25: Somitogenesis switch reactions and their corresponding propensity functions for SSA simulations.

Reaction	Propensity function
$\emptyset \xrightarrow{k_{s1}\text{RALDH2}} R$	$\pi_1 = \Omega \cdot k_{s1} \cdot \text{RALDH2}$
$R + C \xrightarrow{k_{d1}} \emptyset$	$\pi_2 = \frac{k_{d1}RC}{\Omega}$
$R \xrightarrow{k_{d5}} \emptyset$	$\pi_3 = k_{d5}R$
$\emptyset \xrightarrow{V_0} M_C$	$\pi_4 = \Omega \cdot V_0$
$\emptyset \xrightarrow{V_{sc}} M_C$	$\pi_5 = \frac{\Omega \cdot V_{sc}F^n}{(\Omega K_a)^n + F^n}$
$M_C \xrightarrow{k_{d3}} \emptyset$	$\pi_6 = k_{d3}M_C$
$C \xrightarrow{k_{s2}} C$	$\pi_7 = k_{s2}M_C$
$C \xrightarrow{k_{d2}} \emptyset$	$\pi_8 = k_{d2}C$
$\emptyset \xrightarrow{k_{s3}M_0A/L} F$	$\pi_9 = \frac{\Omega \cdot k_{s3} \cdot (M_0A/L) \cdot (\Omega K_I)^m}{(\Omega K_I)^m + R^m}$
$F \xrightarrow{k_{d4}} \emptyset$	$\pi_{10} = k_{d4}F$

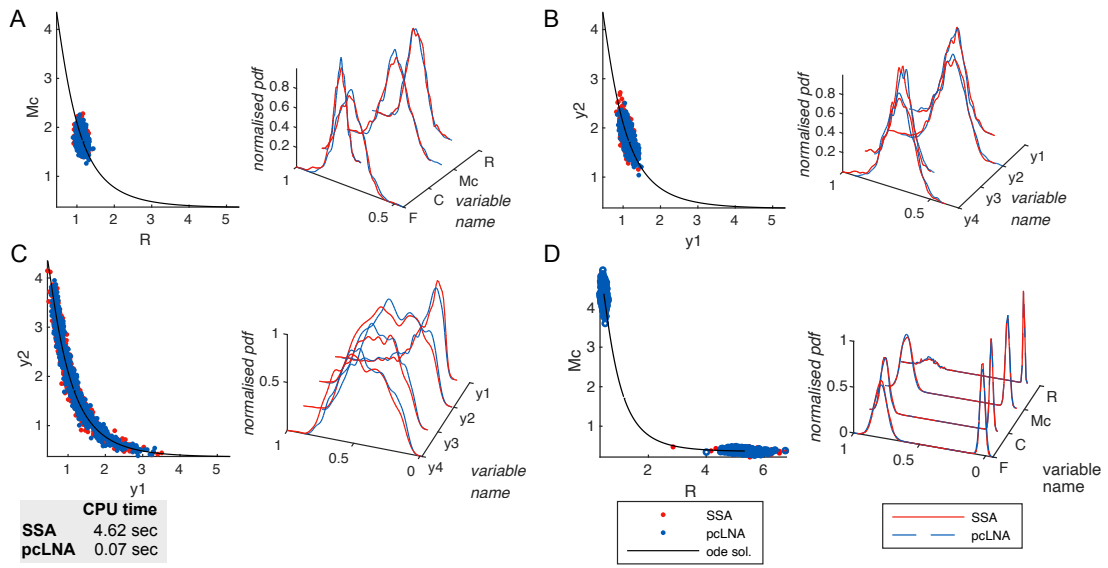


Figure S21: Comparison between SSA (red) and pcLNA (blue) for the somitogenesis switch network at $\Omega = 300$. Panels (A)–(D) correspond to times $t = 2, 5, 20, 99$, respectively. Each panel shows (left) the states recorded at time t of the simulations with solutions of the corresponding RRE, and (right) the corresponding empirical probability density functions of each system variable. The initial conditions for the two ODE solutions are provided in Table S22, and the parameter values are given in Table S23.